

A Unified Framework for Probabilistic Dynamic-, Trajectory- and Vision-based Virtual Fixtures

Maximilian Mühlbauer^{1,2}, Freek Stulp², Sylvain Calinon^{3,4}, Alin Albu-Schäffer^{2,1}, João Silvério²

Abstract—Probabilistic Virtual Fixtures (VFs) enable the adaptive selection of the most suitable haptic feedback for each phase of a task, based on learned or perceived uncertainty. While keeping the human in the loop remains essential, for instance, to ensure high precision, partial automation of certain task phases is critical for productivity. We present a unified framework for probabilistic VFs that seamlessly switches between manual fixtures, semi-automated fixtures (with the human handling precise tasks), and full autonomy. We introduce a novel probabilistic Dynamical System-based VF for coarse guidance, enabling the robot to autonomously complete certain task phases while keeping the human operator in the loop. For tasks requiring precise guidance, we extend probabilistic position-based trajectory fixtures with automation allowing for seamless human interaction as well as geometry-awareness and optimal impedance gains. For manual tasks requiring very precise guidance, we also extend visual servoing fixtures with the same geometry-awareness and impedance behaviour. We validate our approach experimentally on different robots, showcasing multiple operation modes and the ease of programming fixtures.

Index Terms—Human-Centered Automation, Space Robotics and Automation, Learning and Adaptive Systems, Telerobotics and Teleoperation.

I. INTRODUCTION

VIRTUAL Fixtures (VFs) [1], [2] guide humans through tasks by providing haptic feedback. They have been applied to diverse areas such as medical robotics [3], manufacturing on Earth [4] and in space applications [5]–[8] and underwater manipulation [9]. Depending on the task phase, fixtures can be based on different perceptual input, e.g., on robot position or visual measurements [7], [8]. A main limitation of state-of-the-art VFs is however that tasks cannot be accomplished without a human in the loop, raising the need for fixtures that can progress autonomously by outputting actions, e.g. velocities, while still keeping the human in full control. Having a set of complementary fixtures with different input modalities, output types and models, as summarized in Table I, a principled arbitration between them is required. The main contribution of our work is a framework for the fusion of probabilistic fixtures, ensuring both an optimal guidance for the human and automated operation when needed. A novel set of VFs, providing different types of assistance depending on required guidance precision (Table I), forms the backbone of our framework. Common to all our VFs is that they output

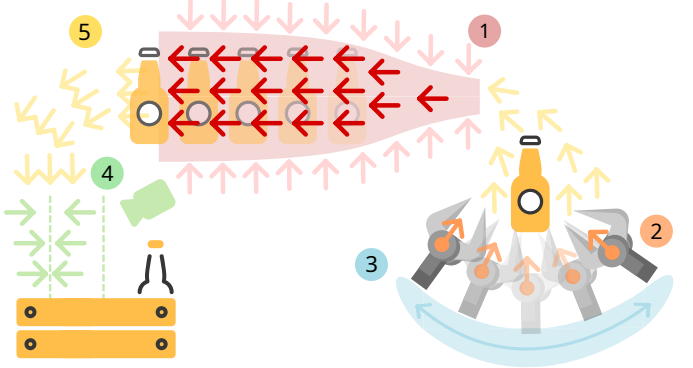


Fig. 1: Overview of the proposed unified framework. [1] (yellow): The combination of all fixture types through probabilistic fusion of Cartesian wrenches to deliver optimal assistance. [2] (red): A new class of learned, Dynamical System based virtual fixtures to assist an operator in progressing along the task while staying near training data. [3] (orange): A novel variable stiffness formulation applicable to position-based fixtures with varying (e.g. cylindrical) geometries [4] (blue). [5] (green): An improved formulation of visual servoing fixtures building on [4] to account for non-Euclidean geometries.

a probabilistic wrench with covariance in pose space. This allows to formulate this fusion of different VFs in a principled way using an arbitration scheme (Section IV-A), thus solving the problem of selecting and switching between VF in a flexible and adaptive manner based on learned and/or perceived uncertainties. An illustration of concurrently active fixtures provided by our framework, fused through such arbitration policy, can be seen in Fig. 1.

To create automated VFs, we propose a novel probabilistic VF for **coarse guidance** based on learned *Dynamical Systems* (DSs) [10], [11] which have been studied extensively in robotics [12]–[20] and are a promising approach to model a wide range of autonomously executed tasks. Commonly, they are equipped with a single attractor and the method ensures that the system converges to that point. Using probabilistic methods providing epistemic uncertainty we model DSs that do not necessarily converge to a single attractor but may also contain recurring motions and can be composed of multiple demonstrated dynamics in different areas of the robot’s workspace while supporting user interaction (Section V).

While DS-based fixtures offer a very flexible automated assistance, probabilistic *position-based trajectory fixtures* are better suited for **precise guidance** when a demonstrated path has to be followed. Although such fixtures are abundant in the literature [8], [21], in scenarios of potential data scarcity, learning efficiency becomes crucial. To facilitate data efficient learning when object and task geometries are known, we propose an extension of a state-of-the-art formulation [22] to

¹ School of Computation, Information and Technology, Sensor Based Robotic Systems and Intelligent Assistance Systems, Technical University of Munich, Friedrich-Ludwig-Bauer-Str. 3, Garching, Germany.

² German Aerospace Center (DLR), Robotics and Mechatronics Center (RMC), Münchener Str. 20, 82234 Weßling, Germany.

³ Idiap Research Institute, Martigny, Switzerland.

⁴ École Polytechnique Fédérale de Lausanne (EPFL), Switzerland.

TABLE I: TYPES OF FIXTURES CONSIDERED IN OUR FRAMEWORK.

Fixture	Input	Output	Accuracy	Workspace
<i>Dynamical System (V)</i>	Pose	Velocity	Coarse	Everywhere
<i>Position-based Trajectory (VI)</i>	Pose	Pose	Fine	Near trajectory
<i>Visual servoing (VII)</i>	Image	Pose	Very fine	Near target

take different geometries into account (Section III-A). Furthermore, as the preferred direction of such VF is known from demonstration data, we automate the execution of such fixtures by extending them with a novel control scheme inspired by the DS based VF (Section VI).

For **very precise guidance**, particularly near relevant objects or targets in the robot workspace, we leverage probabilistic visual measurements. The *visual servoing fixture* formulation [8] can help to arbitrate between multiple possible targets. We extend this formulation to cylindrical and spherical manifolds, taking special arrangements of those targets into account (Section VII).

Both *position-* and *vision-based fixtures* rely on an impedance control scheme, pulling the end effector towards a probabilistic attractor point. As this attractor point may exhibit significant uncertainty in some directions, previously, variable stiffness formulations have been employed to modulate the controller stiffness accordingly [8]. Currently available stiffness scaling methods however fail to model couplings between positional and rotational degrees of freedom (DoFs). We therefore propose a novel method to derive a stiffness matrix from the fixture’s covariance, taking all possible couplings into account (Section IV-B).

Our proposed probabilistic VF framework allows to reproduce the whole range of automation levels, starting with teleoperation aided by VFs over partial automation, where the human operator still performs certain tasks, up to full automation. The key contributions of our work are the following:

- 1) An extended arbitration scheme taking different types of VFs and different underlying geometries into account (Section IV-A);
- 2) A novel dynamical system based VF (Section V);
- 3) A novel variable stiffness formulation allowing to model couplings between positional and orientational DoFs (Section IV-B);
- 4) An extension of position-based fixtures to different manifolds as well as their automation (Section VI);
- 5) An extension of visual servoing fixtures to different manifolds (Section VII).

For evaluating our framework, we have implemented it on different robotic systems under different automation levels. After experimentally validating the individual fixtures (Sections VIII-A to VIII-D), we evaluate the combination of fixtures both in partially automated scenarios with human interaction (Sections VIII-F and VIII-G) as well as in a fully automated scenario on a space-ready robot (Section VIII-E).

II. RELATED WORK

Our approach builds upon a range of techniques from robot learning and control which we review in this section. The proposed DS-based VF formulation (Section V) builds on the learning of DS body of work [10], [11], [15], [18] as well

as on methods for human interaction with them explored in Sections II-A and II-B. For position-based trajectory fixtures (Section VI), related automation approaches (Section II-C) as well as adaptive stiffness scaling (Section II-E) are explored. Finally, we review existing techniques for the adaptive arbitration of VFs in Section II-D.

A. Dynamical Systems

Dynamical Systems (DSs) model actions as a function of the system state. As such, they can for example encode velocity policies $\dot{x} = f(x)$. Dynamic Movement Primitives (DMPs) [10], [11] model such systems with a single attractor by combining a stable attractor dynamic with forcing terms. Those forcing terms deform the attractor field to e.g. follow complex trajectories. A DMP can be learned by optimizing the parameters of its forcing terms to follow a set of demonstrations as closely as possible. For an overview of popular DMP-based approaches, the reader is referred to [12].

Stable Estimators of Dynamical Systems (SEDS) [15] learns a Gaussian Mixture Model (GMM) and ensures stability of the resulting DS towards an attractor point. For the case of multiple attractors, [16] proposes a clustering method. For complex DSs, [17] proposes to learn the non-linearity of the DS, allowing for an easy adaptation of the learned dynamics with the use case of obstacle avoidance. Learning implicit manifolds promises to better model complex DSs [14]. Neural networks allow for even more powerful estimations of DSs. In [18], global stability of the learned system is ensured through a special network architecture. Other approaches [19], [20] design a special loss function to shape the learned system. At the cost of a loss of a global stability proof, the more powerful expressivity of deep neural networks can be leveraged. Closest to our approach are [23]–[25] which also utilize a stabilizing policy together with the learned nonparametric velocity field. They however integrate the velocity field to positions, leaving user interaction for future work which our methods allows for.

While ensuring convergence to an attractor point, many of the proposed methods exhibit motions which were not demonstrated when far away from demonstrated data and therefore might surprise the operator. Furthermore, it is not possible to fuse multiple of such motion policies in one unified framework. We here propose a non-parametric approach based on Kernelized Movement Primitives (KMPs) leveraging the fusion of different policies (Section V). This allows us to have multiple DSs active in the workspace in parallel that can e.g. each handle a specific portion of a task. Our formulation without fixed attractor points also allows to model periodic motions, e.g. limit cycles. A probabilistic stabilizing policy ensures that the robot always stays close to demonstrated data by computing a velocity towards the closest known dynamic. By using appropriate Riemannian distance metrics in the kernel function, we can account for the full pose as state input.

B. User Interaction with Dynamical Systems

Conventionally, DSs are used to program autonomous robot motions. Interactions from a human are treated as perturbations

and therefore cancelled. In contrast, [26] design a DMP for human interaction. The DMP evolution is synchronized with the human movement and a penetrable VF provides force feedback when the user would deviate from the programmed trajectory. Stiffness scaling is used to allow for user corrections. In [27], a similarly time-synchronized DMP is designed allowing for a shared control scheme where the autonomous agent controls repetitive DoFs while the human operator is responsible for the required accuracy in the more variable DoFs. Chen et al. [28] sample attractor points from a DS and employ variable stiffness with impedance control which they also combine with a human operator [29].

Closest to our approach is [30] who hand-program a DS for user interaction. An impedance controller is used for torque control of the robot allowing for human interactions. For force-based tasks, a force overlay is added when the robot is in surface contact. The stabilizing properties of the DS are used to bring the robot back to the surface in case of perturbations.

In general, using learned DSs as haptic aids for human operators has received little attention so far. We aim to fill this gap by employing a damping controller (Section V-C) enabling the guidance of a human operator through a state-based DS. The system state evolves both through the actions of the DS as well as through user input. The probabilistic formulation achieves an optimal fusion of different policies as well as between different VFs.

C. Position-based Trajectory VF Automation

Position-based VFs, which take the robot pose as input and output a desired pose (Table I), have been applied to many teleoperation tasks for example in medical [3], [31] and industrial robotics [32]. They have also been used together with vision [33]. Closest to our work are the probabilistic trajectory fixtures [21], [34]. An overview of different types of fixtures can be found in [2], [35]. Traditionally, VFs constrain the user by keeping them outside of forbidden regions or guiding them along a path without directional guidance [2].

For our framework, an automated version of such fixtures is required. To this end, [36] propose to use the path direction to guide the user along a path. In [3], a cylindrical VF is used to move along a path. For full automation, radius and length of the cylinder are set to 0 which makes the user follow a given trajectory. Automation is achieved by introducing a point mass which is accelerated by a user-defined force - this force is being counteracted by a virtual damping as well as a damping potentially introduced by the user, therefore limiting the maximum velocity. Transitions between different levels of autonomy are possible by enlarging or shrinking the guiding cylinder. None of these approaches however implements more than one concurrently active fixture. Furthermore, no fusion with other types of fixtures is possible with those works. Through a probabilistic fusion, our approach allows to both model multiple concurrently active trajectory fixtures as well as to fuse the automated fixture with other fixtures.

D. Virtual Fixture Arbitration

As shown previously [8], a function to arbitrate between different VFs is required, which extends the concept of *ar-*

bitration between human operator and system (see [37] for a survey). To this end, special controllers to stabilize hard switches [38] or hand-tuned weights [7], [39] can be used. One major limitation of these works is that the arbitration function or stabilizing controller does not make use of information from the fixtures but instead needs to be handcrafted.

This limitation can be resolved using probabilistic formulations [21]. Further extensions allow for an individual weighting along all DoFs instead of a single scalar weight value. This can also be used to arbitrate between system and human operator [34], [40]. In a previous work [8] a Gaussian product has been used to perform DoF-specific arbitration. We build on this foundation to include all fixtures highlighted in Table I in a unified framework, showing how DS based VFs (Section V) and VFs on different geometries can be fused (Section IV-A).

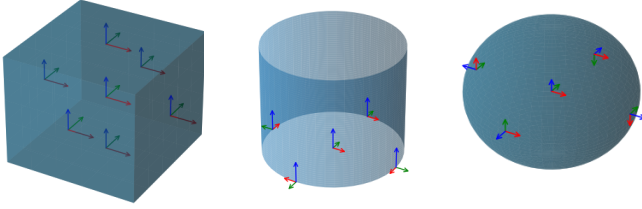
E. Virtual Fixtures with Variable Stiffness

Impedance control [41] allows for compliant interaction with the environment and is therefore crucial for safe manipulation as well as robot-human interaction. A key element of this approach is the choice of stiffness matrix, as this matrix determines the relationship between position offset and exerted forces. This key property can be changed according to the task needs using variable stiffness formulations.

To this end, [40] suggest to learn the coupling stiffness for teleoperation. Learned from task properties, the coupling between input device and remote robot is realized with a low stiffness for safe interactions or with high stiffness to achieve a high tracking accuracy. Other approaches [28], [29] learn a DS with variable stiffness along an orthogonal to the motion direction and furthermore demonstrate it in a shared control application. The approach is also extended to incorporate a learned stiffness for rotational DoFs [42].

Closer to our requirements is [43] where based on the uncertainty of a perception algorithm, the stiffness of the robot controller is adapted through a scaling factor. Covariance matrices can however model complex relationships between the individual DoFs which cannot be represented by a scalar factor. In [44], a block diagonal matrix with submatrices for position and orientation stiffness based on the covariance matrix of a learned trajectory is used. While this choice of stiffness matrix can model a wide range of stiffness behaviours, couplings between positional and orientational DoFs which e.g. full covariance matrices can represent are neglected.

As our experiments underline (Section VIII-A), covariance matrices with couplings between position and orientation are important for variable stiffness control. Note that simply using a scaled version of the precision matrix $\mathbf{P} = \mathbf{\Sigma}^{-1}$ is not possible as this might lead to too high stiffness values that might render a physical system unstable. We therefore build upon the findings of [45], [46] who decompose a stiffness matrix into eigenscrews. This can be performed similarly using precision matrices to design a desired stiffness matrix with such couplings while respecting stiffness limits (Section IV-B).



(a) $\mathcal{M}_1: \mathbb{R}^3 \times \mathcal{S}^3$. (b) $\mathcal{M}_2: \mathcal{S}^1 \times \mathbb{R}^2 \times \mathcal{S}^3$. (c) $\mathcal{M}_3: \mathcal{S}^2 \times \mathbb{R}^1 \times \mathcal{S}^3$.

Fig. 2: Coordinate systems used in this work inspired by and using the notation of [22]. Depending on the task, properties can be expressed more efficiently in cylindrical (\mathcal{M}_2) or spherical (\mathcal{M}_3) compared to Cartesian (\mathcal{M}_1) coordinates. The coordinate systems in each image depict the orientation basis, i.e. the unit quaternion $(0, 0, 0, 1)^\top$ for different positions on the manifold.

III. BACKGROUND

A. Riemannian Manifolds and Probabilities

The geometry of a task can be modeled using Riemannian manifolds – this is already required for orientations which are non-Euclidean. A full pose \mathbf{x} can therefore be expressed by the product of manifolds representing a 3-dimensional position and the unit quaternion.¹ Following the notation of [22], we consider the manifolds \mathcal{M} shown in Fig. 2 in this work:

- 1) \mathcal{M}_1 with $\mathbf{x} \in \mathbb{R}^3 \times \mathcal{S}^3$: We use this manifold to represent Cartesian poses as product of the position expressed in 3-dimensional Euclidean space and a unit quaternion.
- 2) \mathcal{M}_2 with $\mathbf{x} \in \mathcal{S}^1 \times \mathbb{R}^2 \times \mathcal{S}^3$: This manifold represents cylindrical poses as product of the angle ϕ from the x -axis, the radius r measured as distance from the origin in the xy plane and the z coordinate and a unit quaternion. The base of the orientation is adjusted such that its y axis is always pointing in direction of increasing radius.
- 3) \mathcal{M}_3 with $\mathbf{x} \in \mathcal{S}^2 \times \mathbb{R}^1 \times \mathcal{S}^3$: We use this manifold to represent spherical poses as product of the angles from the x and z axis (often denoted as *azimuthal* angle ϕ and *polar* angle θ), the radius r and a unit quaternion. The base of the orientation is adjusted such that the z axis is always pointing in direction of increasing radius.

The manifold logarithm $\text{Log}_{\mathbf{x}_1}^{\mathcal{M}} \mathbf{x}_2$ on \mathcal{M} calculates the tangent vector $\mathbf{u}_{12} \in \mathcal{T}_{\mathbf{x}_1} \mathcal{M}$ from \mathbf{x}_1 in the direction of \mathbf{x}_2 , its magnitude is equal to the geodesic distance between the points. Its inverse, the manifold exponential $\text{Exp}_{\mathbf{x}_1}^{\mathcal{M}} \mathbf{u}_{12}$, allows to recover \mathbf{x}_2 on the manifold. Parallel transport is required to move vectors between different tangent spaces centered at \mathbf{x}_i . The reader is referred to [47], [48] for a more exhaustive treatment of these Riemannian operations. Between tangent spaces of different manifolds, manifold-specific Jacobians $\mathbf{J}_{\mathcal{M}}$ (see Appendix E) transform vectors *contravariantly* [49].

With the logarithm map and the Gaussian distribution proposed by [47], [48], we compute the probability of \mathbf{x} to

$$\mathcal{N}(\mathbf{x} | \boldsymbol{\mu}, \boldsymbol{\Sigma}) = \frac{1}{\sqrt{(2\pi)^d |\boldsymbol{\Sigma}|}} e^{-\frac{1}{2} \text{Log}_{\boldsymbol{\mu}}^{\mathcal{M}}(\mathbf{x})^\top \boldsymbol{\Sigma}^{-1} \text{Log}_{\boldsymbol{\mu}}^{\mathcal{M}}(\mathbf{x})}, \quad (1)$$

which is parameterized by a mean $\boldsymbol{\mu} \in \mathcal{M}$ and a covariance matrix $\boldsymbol{\Sigma} \in \mathbb{R}^{6 \times 6}$ in the tangent space $\mathcal{T}_{\boldsymbol{\mu}} \mathcal{M}$.

¹To avoid issues with \mathcal{S}^3 double-covering $SO(3)$, we wrap the logarithm at a full rotation, ensuring that $\text{Log}_{\mathbf{q}}(-\mathbf{q}) = \mathbf{0}$.

Finally, a weighted distance measure between \mathbf{x}_1 and \mathbf{x}_2 is often required. For this, we define the on-manifold distance

$$\begin{aligned} d_{\mathbf{A}}^{\mathcal{M}}(\mathbf{x}_1, \mathbf{x}_2) &= \left\| \text{Log}_{\mathbf{x}_1}^{\mathcal{M}} \mathbf{x}_2 \right\|_{\mathbf{A}}^2 \\ &= \text{Log}_{\mathbf{x}_1}^{\mathcal{M}}(\mathbf{x}_2)^\top \mathbf{A} \text{Log}_{\mathbf{x}_1}^{\mathcal{M}}(\mathbf{x}_2). \end{aligned} \quad (2)$$

with a weighting matrix \mathbf{A} expressed in tangent space $\mathcal{T}_{\mathbf{x}_1} \mathcal{M}$.

B. Impedance-controlled Virtual Fixtures

Our Virtual Fixtures framework outputs a Cartesian wrench \mathbf{w}_{VF} which is applied to the robot's end effector (Section IV). Assuming a gravity-compensated, torque-controlled manipulator, the corresponding desired joint torques evaluate to

$$\boldsymbol{\tau} = \mathbf{J}^\top \mathbf{w}_{\text{VF}}. \quad (3)$$

Note that \mathbf{w}_{VF} is a covector in cotangent space $\mathcal{T}_{\mathbf{x}_{\text{ee}}}^* \mathcal{M}$ ($\eta: \mathcal{T}_{\mathbf{x}_{\text{ee}}} \mathcal{M} \rightarrow \mathbb{R}$) requiring the covariant transformation with $\mathbf{J}_{\mathcal{M}}^\top$ [49] following from the conservation of power $\boldsymbol{\tau}^\top \dot{\mathbf{q}} = \mathbf{w}^\top \dot{\mathbf{x}}$. We assume that \mathbf{w}_{VF} is a combination of $N_{\text{VF}} = N_{\text{DS}} + N_{\text{PB}} + N_{\text{VS}}$ individual wrenches associated with different VFs. For position-based VFs (Section VI), this wrench is computed as

$$\mathbf{w}_{\text{VF},i} = \mathbf{K}_{\text{VF},i} \text{Log}_{\mathbf{x}_{\text{ee}}}^{\mathcal{M}}(\mathbf{x}_{\text{VF},i}) + \mathbf{D}_{\text{VF},i} \frac{d}{dt} \text{Log}_{\mathbf{x}_{\text{ee}}}^{\mathcal{M}}(\mathbf{x}_{\text{VF},i}), \quad (4)$$

where $\mathbf{x}_{\text{ee}} \in \mathcal{M}$ is the end effector pose. $\mathbf{K}_{\text{VF},i}$, $\mathbf{D}_{\text{VF},i}$ and $\mathbf{x}_{\text{VF},i}$ are the stiffness, damping and attractor of the fixture. $\text{Log}_{\mathbf{x}_{\text{ee}}}^{\mathcal{M}}(\mathbf{x}_{\text{VF}})$ denotes the manifold logarithm [47] of \mathbf{x}_{VF} at \mathbf{x}_{ee} , which is the on-manifold equivalent to the Euclidean $\mathbf{x}_{\text{VF},i} - \mathbf{x}_{\text{ee}}$, taking orientation and different manifolds \mathcal{M} into account. $\frac{d}{dt} \text{Log}_{\mathbf{x}_{\text{ee}}}^{\mathcal{M}}(\mathbf{x}_{\text{VF}})$ is the corresponding time derivative. We compute a single Cartesian wrench \mathbf{w}_{VF} to be used in (3) from multiple individual impedance- as well as velocity-controlled fixtures $\mathbf{w}_{\text{VF},i}$ on different manifolds through a probabilistic fusion (Section IV-A).

C. Probabilistic Learning from Demonstration

Different probabilistic models encoding assistive behaviors can be learned from demonstration data using Gaussian distributions. We are specifically interested to model both the *aleatoric* uncertainty which is inherent to the data, i.e. the variability in demonstrations, as well as the *epistemic* uncertainty, which is the uncertainty caused by a lack of data. We argue that fixture activation should be inversely proportional to uncertainty – both epistemic and aleatoric – such that strong guidance corresponds to low uncertainty levels.

GMMs [48], [50] encode the joint distribution between input \mathbf{x} and output \mathbf{y} with M Gaussians, i.e.

$$\begin{bmatrix} \mathbf{x} \\ \mathbf{y} \end{bmatrix} \sim \sum_{m=1}^M \pi_m \mathcal{N} \left(\begin{bmatrix} \mathbf{x} \\ \mathbf{y} \end{bmatrix} \middle| \boldsymbol{\mu}_m, \boldsymbol{\Sigma}_m \right). \quad (5)$$

Using Gaussian Mixture Regression (GMR), the conditional distribution of \mathbf{y} given the input \mathbf{x} can be computed as

$$p(\mathbf{y} | \mathbf{x}) = \sum_{m=1}^M \pi_m(\mathbf{x}) \mathcal{N}(\mathbf{y} | \boldsymbol{\mu}_{m|\mathbf{x}}, \boldsymbol{\Sigma}_{m|\mathbf{x}}). \quad (6)$$

Note that this is a Mixture of Experts (MoE) [51] model, computing a multi-modal weighted sum of different experts

represented by Gaussian distributions in an “or” operation. Subsequently, a unimodal approximation can be computed as

$$p(\mathbf{y}|\mathbf{x}) = \mathcal{N}(\mathbf{y}|\boldsymbol{\mu}_{\text{GMR}}, \boldsymbol{\Sigma}_{\text{GMR}}) \quad (7)$$

which can then, for example, be used in the position-based trajectory fixture (Section VI) where time as input and pose as output are jointly encoded. The reader is referred to [50] for details of the computation in (5) – (7). We use the on-manifold Gaussian operations from [47]. The GMM encodes *aleatoric* uncertainty, the resulting covariance matrix can therefore be used to scale the stiffness (Section IV-B) of a fixture to allow the operator to reproduce this encoded variability.

Kernel-based methods such as Gaussian Processes (GPs) [52] and KMPs [53] are well-known in imitation learning for representing *epistemic* uncertainty. Notably, the latter is capable of capturing *both* aleatoric and epistemic uncertainties. With these methods, particularly when using stationary kernels (e.g., squared-exponential or Matérn), the predicted uncertainty increases with the distance between training data and new inputs. This is used in the DS-based VF (Section V) to find validity regions for learned dynamics. In KMPs, a function $\mathbf{y}(\mathbf{x})$ is approximated via a weighted superposition of basis functions $\mathbf{y}(\mathbf{x}) = \boldsymbol{\Theta}(\mathbf{x})^\top \mathbf{w}$, where $\boldsymbol{\Theta}(\mathbf{x})$ is a matrix of basis functions and \mathbf{w} is a vector of normally distributed weights, $\mathbf{w} \sim \mathcal{N}(\boldsymbol{\mu}_w, \boldsymbol{\Sigma}_w)$, resulting in a parametric trajectory distribution. It further assumes that a probabilistic reference trajectory distribution $\{\boldsymbol{\mu}_n, \boldsymbol{\Sigma}_n\}_{n=1}^N$ extracted from a dataset of observations of \mathbf{x} , \mathbf{y} using GMM/GMR at inputs \mathbf{x}_n is available. By minimizing the KL divergence between parametric and reference trajectory distributions and applying the kernel trick $\mathbf{k}(\mathbf{x}_i, \mathbf{x}_j) = \boldsymbol{\Theta}(\mathbf{x}_i)^\top \boldsymbol{\Theta}(\mathbf{x}_j) = k(\mathbf{x}_i, \mathbf{x}_j) \mathbf{I}$, where $k(\mathbf{x}_i, \mathbf{x}_j)$ is a kernel function, the mean and covariance prediction of a KMP are computed, for a test point \mathbf{x}^* , as

$$\boldsymbol{\mu}^* = \mathbf{K}(\mathbf{x}^*, \mathbf{x}) (\mathbf{K}(\mathbf{x}, \mathbf{x}) + \lambda \boldsymbol{\Sigma})^{-1} \boldsymbol{\mu} \quad (8)$$

$$\boldsymbol{\Sigma}^* = \alpha (\mathbf{K}(\mathbf{x}^*, \mathbf{x}^*) - \mathbf{K}(\mathbf{x}^*, \mathbf{x}) (\mathbf{K}(\mathbf{x}, \mathbf{x}) + \lambda_c \boldsymbol{\Sigma})^{-1} \mathbf{K}(\mathbf{x}, \mathbf{x}^*)) \quad (9)$$

where λ , λ_c and α are regularization and scaling hyperparameters and $\boldsymbol{\mu} = [\boldsymbol{\mu}_1^\top, \dots, \boldsymbol{\mu}_N^\top]^\top$, $\boldsymbol{\Sigma} = \text{blockdiag}(\boldsymbol{\Sigma}_1, \dots, \boldsymbol{\Sigma}_N)$. Please see [53] for a detailed derivation. Note the connection between GPs and KMPs, where in classical GPs [52] we have $\lambda_c = \lambda$ and $\boldsymbol{\Sigma} = \mathbf{I}$ (*homoscedasticity*), $\alpha = 1$ and $\boldsymbol{\mu}$ are directly the observations \mathbf{y} .

As both GPs and KMPs require kernels, a special treatment for manifold-valued input data is required. We therefore use (2) to calculate the on-manifold distance with weight $\mathbf{A} = \mathbf{I}$. Note that this distance is only valid for sufficiently close \mathbf{x}_1 and \mathbf{x}_2 . This is a reasonable assumption in our VF approach, as the expected level of assistance is inversely proportional to the distance between inputs. More complex treatments might be required depending on the manifold and input data [54].

By treating the output of GMMs and KMPs as experts, they can be fused using a Product of Experts (PoE) [55] in an “and” operation where the constraints of each expert are satisfied approximately. As we will see in the next section, this allows to arbitrate between different VFs, even if they do not share the same underlying representation.

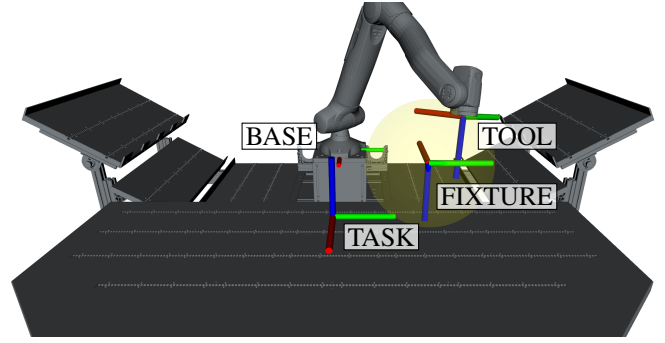


Fig. 3: Coordinate systems used by our method. The task coordinate system [TASK] defined with respect to the robot base [BASE] allows to account for different object placements in the workspace while the specification of fixture coordinate systems [FIXTURE] relative to the [TASK] coordinate system is crucial for cylindrical and spherical coordinates. Finally, the tool frame [TOOL] depends on the current end effector pose of the robot.

IV. VIRTUAL FIXTURE FRAMEWORK

We assume that depending on the specific task at hand, Virtual Fixtures with different properties are required to optimally guide an operator or for automating the task. Table I summarizes the properties of the individual VFs we consider in this work. Common for all fixtures we propose is that their wrenches are modeled as random variables with on-manifold, multivariate Gaussian densities

$$p(\mathbf{w}_{\text{VF},i}) = \mathcal{N}(\boldsymbol{\mu}_{\text{VF},i}, \boldsymbol{\Sigma}_{\text{VF},i}) \quad (10)$$

where $\boldsymbol{\mu}_{\text{VF},i}$ is the mean of the wrench calculated by each fixture in its specific coordinate system (Fig. 2), under the assumption that $\mathbf{x}_{\text{VF},i}$ is Gaussian-distributed. This allows for a natural arbitration between the individual fixtures using their uncertainty expressed by the covariance $\boldsymbol{\Sigma}_{\text{VF},i}$, taking also DoF-specific uncertainty and correlations into account.

Figure 3 shows the different coordinate systems used by our method. An easy transfer between different object placements is possible through the task coordinate system. Coordinates for individual fixtures placed relative to this coordinate system allow us to exploit the properties of different geometries.

A. Virtual Fixture Arbitration

Previous works [8] use a PoE [55] to perform the arbitration of different fixture wrenches expressed in the same coordinate system. Extending this, we furthermore consider the fixture-specific coordinate systems depicted in Fig. 2. Each fixture outputs a mean wrench $\boldsymbol{\mu}_{\text{VF},i,\mathcal{M}}$ in the cotangent space $\mathcal{T}_{\mathbf{x}_{\text{ee}}}^* \mathcal{M}$ of a specific coordinate systems \mathcal{M} through (4). This prohibits a direct fusion of the fixture wrenches as the entries in the wrench covector correspond to different DoFs. In order to stay robot agnostic, we propose to transform covariances and mean wrenches into the (co)tangent space $\mathcal{T}_{\mathbf{x}_{\text{ee}}}^{(*)} \mathcal{M}_1$ using

$$\boldsymbol{\mu}_{\text{VF},i,\mathcal{M}_1} = \mathbf{J}_{i,\mathcal{M}}^\top \boldsymbol{\mu}_{\text{VF},i,\mathcal{M}} \quad (11)$$

$$\boldsymbol{\Sigma}_{\text{VF},i,\mathcal{M}_1} = \mathbf{J}_{i,\mathcal{M}}^{-1} \boldsymbol{\Sigma}_{\text{VF},i,\mathcal{M}} \mathbf{J}_{i,\mathcal{M}}^{-\top} \quad (12)$$

with the manifold Jacobian $\mathbf{J}_{i,\mathcal{M}} = \frac{\partial \mathbf{x}_{\text{ee},i,\mathcal{M}}}{\partial \mathbf{x}_{\text{ee},\mathcal{M}_1}}$ [56] given in Appendix F. This corresponds to the transformation of the

covector $\boldsymbol{\mu}_{\text{VF},i}$ from $\mathcal{T}_{x_{ee}}^* \mathcal{M}$ into $\mathcal{T}_{x_{ee}}^* \mathcal{M}_1$ as well as of the twice contravariant tensor $\boldsymbol{\Sigma}_{\text{VF}}$ from $\mathcal{T}_{x_{ee}} \mathcal{M}$ into $\mathcal{T}_{x_{ee}} \mathcal{M}_1$.

The wrench $\boldsymbol{\mu}_{\text{VF},i,\mathcal{M}_1}$ in cotangent space $\mathcal{T}_{x_{ee}}^* \mathcal{M}_1$ expresses the forces of the wrench in the **FIXTURE** coordinate system while the torques are expressed in **TOOL** coordinates (Fig. 3). Compared to that, the SE(3) wrench required by (3) expects also the forces in **TOOL** coordinates which corresponds to a rotation of the position part of the tangent space. The mean wrench $\boldsymbol{\mu}_{\text{VF},i}$ of each fixture i to be commanded at the end effector is thus transformed from $\mathcal{T}_{x_{ee}}^* \mathcal{M}_1$ to $\mathfrak{se}(3)$ using

$$\boldsymbol{\mu}_{\text{VF},i,\text{SE3}} = \begin{bmatrix} \mathbf{R}_{ee}^\top & \mathbf{0} \\ \mathbf{0} & \mathbf{I} \end{bmatrix} \boldsymbol{\mu}_{\text{VF},i,\mathcal{M}_1}, \quad (13)$$

where \mathbf{R}_{ee} expresses the rotation of x_{ee} in the fixture's coordinate system. The same rotation has to be applied to the covariance matrix of the fixture as well

$$\boldsymbol{\Sigma}_{\text{VF},i,\text{SE3}} = \begin{bmatrix} \mathbf{R}_{ee}^\top & \mathbf{0} \\ \mathbf{0} & \mathbf{I} \end{bmatrix} \boldsymbol{\Sigma}_{\text{VF},i,\mathcal{M}_1} \begin{bmatrix} \mathbf{R}_{ee} & \mathbf{0} \\ \mathbf{0} & \mathbf{I} \end{bmatrix}. \quad (14)$$

The aligned Cartesian mean wrench and covariance matrices can then be used as experts in a PoE (cf. [8]) to calculate the arbitrated wrench as result of the optimization

$$\hat{\boldsymbol{w}} = \arg \min_{\boldsymbol{w}} \sum_{i=1}^{N_{\text{VF}}} (\boldsymbol{w} - \boldsymbol{\mu}_{\text{VF},i,\text{SE3}})^\top \boldsymbol{\Sigma}_{\text{VF},i}^{-1} (\boldsymbol{w} - \boldsymbol{\mu}_{\text{VF},i,\text{SE3}}), \quad (15)$$

solved as product of $N_{\text{VF}} = N_{\text{DS}} + N_{\text{PB}} + N_{\text{VS}}$ Gaussians

$$\hat{\boldsymbol{w}} = \hat{\boldsymbol{\Sigma}}_{\text{VF}} \sum_{i=1}^{N_{\text{VF}}} \boldsymbol{\Sigma}_{\text{VF},i}^{-1} \boldsymbol{w}_{\text{VF},i}, \quad \hat{\boldsymbol{\Sigma}} = \left(\sum_{i=1}^{N_{\text{VF}}} \boldsymbol{\Sigma}_{\text{VF},i}^{-1} \right)^{-1}. \quad (16)$$

The resulting $\hat{\boldsymbol{w}}$ is then applied to the robot through (3).

B. Variable Impedance Control

Modulating the controller stiffness, as a form of authority allocation, allows to assign a higher importance to the fixture in case of low uncertainty and give the operator more freedom otherwise. Using a full covariance matrix, our fixtures can also express DoF specific as well as coupled uncertainties. For reproducing these properties in the robot's impedance behaviour, we propose a method to match the stiffness matrix characteristics to those of the covariance matrix. Unlike previous works [43], [44], we aim to create a full stiffness matrix with nonzero coupling terms \mathbf{K}_{tr}

$$\mathbf{K} = \begin{bmatrix} \mathbf{K}_t & \mathbf{K}_{tr} \\ \mathbf{K}_{tr}^\top & \mathbf{K}_r \end{bmatrix}. \quad (17)$$

A first approach could compute the stiffness to $\mathbf{K}_i = k \boldsymbol{\Sigma}_{\text{VF},i}^{-1}$ where k is used to scale the precision matrix. Such approach is however too naive, as it fails to respect maximum stiffness values attainable in a robotic system. Furthermore, the vastly different scales of stiffness values for translation (e.g. 2000 $\frac{\text{N}}{\text{m}}$) and rotation (e.g. 50 $\frac{\text{Nm}}{\text{rad}}$) are neglected.

We therefore propose to decompose the covariance matrix $\mathbf{P}_{\text{VF},i}$ and reassemble it to a stiffness matrix while preserving its properties to the extent possible. Building on the findings of [57], [58] on the decomposition of spatial stiffness matrices,

we decompose a rotated precision matrix $\mathbf{P}'_{\text{VF},i}$ into translational ($\mathbf{P}_{t,\text{VF},i}$) and rotational ($\mathbf{P}_{r,\text{VF},i}$) components

$$\mathbf{P}'_{\text{VF},i} = \begin{bmatrix} \mathbf{A} & \mathbf{B} \\ \mathbf{B}^\top & \mathbf{C} \end{bmatrix} = \mathbf{P}_{t,\text{VF},i} + \mathbf{P}_{r,\text{VF},i} = \begin{bmatrix} \mathbf{A} & \mathbf{B} \\ \mathbf{B}^\top & \mathbf{B}^\top \mathbf{A}^{-1} \mathbf{B} \end{bmatrix} + \begin{bmatrix} \mathbf{0} & \mathbf{0} \\ \mathbf{0} & \mathbf{C} - \mathbf{B}^\top \mathbf{A}^{-1} \mathbf{B} \end{bmatrix}. \quad (18)$$

$\mathbf{P}_{\text{VF},i}$ is rotated with $\mathbf{R}_{\text{diag},i}$ to obtain

$$\mathbf{P}'_{\text{VF},i} = \begin{bmatrix} \mathbf{R}_{\text{diag},i} & \mathbf{0} \\ \mathbf{0} & \mathbf{R}_{\text{diag},i} \end{bmatrix}^\top \mathbf{P}_{\text{VF},i} \begin{bmatrix} \mathbf{R}_{\text{diag},i} & \mathbf{0} \\ \mathbf{0} & \mathbf{R}_{\text{diag},i} \end{bmatrix} \quad (19)$$

where $\mathbf{R}_{\text{diag},i}$ is chosen such that \mathbf{A} only contains diagonal entries.

$\mathbf{P}_{t,\text{VF},i}$ and $\mathbf{P}_{r,\text{VF},i}$ can be further decomposed and after a scaling be realized using three screw springs and three rotational springs, respectively [57]. An eigendecomposition of $\mathbf{P}_{r,\text{VF},i}$ yields the torsional spring axes ($j = 4, 5, 6$) as eigenvectors $\boldsymbol{w}_j = (0, 0, 0, w_{\text{rx},j}, w_{\text{ry},j}, w_{\text{rz},j})^\top$ and corresponding eigenvalues λ_j . Those eigenvalues allow to compute a scaling

$$s_j = \begin{cases} 0, & \lambda_j < \lambda_{\text{rot}}^- \\ \frac{\lambda_j - \lambda_{\text{rot}}^-}{\lambda_{\text{rot}}^+ - \lambda_{\text{rot}}^-}, & \\ 1, & \lambda_j \geq \lambda_{\text{rot}}^+ \end{cases}, \quad (20)$$

where λ_{rot}^- and λ_{rot}^+ are empirically determined hyperparameters for “low” and “high” eigenvalues which will be translated to full and zero stiffness. The torsional springs are then realized as ($j = 4, 5, 6$)

$$\mathbf{K}'_j = k_{\text{nom},j} s_j \boldsymbol{w}_j \boldsymbol{w}_j^\top \quad (21)$$

with the nominal stiffnesses $\mathbf{k}_{\text{nom}} = (k_t, k_t, k_t, k_r, k_r, k_r)^\top$ where k_t is the nominal translational and k_r the nominal rotational stiffness. Eigenvalues $\geq \lambda_{\text{rot}}^+$ thus result in a nominal stiffness along the corresponding rotational DoF while eigenvalues $< \lambda_{\text{rot}}^-$ result in zero stiffness with linear scaling in between.

The remaining screw springs ($j = 1, 2, 3$) are given by wrench axes $\boldsymbol{w}_j = (e_j^\top, w_{\text{tx},j}, w_{\text{ty},j}, w_{\text{tz},j})^\top$ with $[e_1 \ e_2 \ e_3] = \mathbf{I}_3$ and corresponding λ_j from the diagonal entries of \mathbf{A} in \mathbf{P}_t . The scaling s_j of (20) is also computed for those springs with factors λ_{trans}^- and λ_{trans}^+ . We furthermore ensure that the rotational entries of \boldsymbol{w}_j do not get a too high stiffness by limiting

$$s_j \leq \frac{k_r}{k_{\text{nom},j} \sqrt{w_{\text{tx},j}^2 + w_{\text{ty},j}^2 + w_{\text{tz},j}^2}}. \quad (22)$$

While this operation also impacts the coupling introduced by the screw spring, it ensures that the resulting stiffness matrix is realizable and still as close as possible to the original precision matrix $\mathbf{P}_{\text{VF},i}$. Finally, the wrench springs are also realized to ($j = 1, 2, 3$)

$$\mathbf{K}'_j = k_{\text{nom},j} s_j \boldsymbol{w}_j \boldsymbol{w}_j^\top. \quad (23)$$

The resulting stiffness matrix is then calculated from wrench ($j = 1, 2, 3$) and torsional ($j = 4, 5, 6$) springs to

$$\mathbf{K}' = \sum_{j=1}^6 \mathbf{K}'_j \quad (24)$$

and rotated back using

$$\mathbf{K}_i = \begin{bmatrix} \mathbf{R}_{\text{diag},i} & \mathbf{0} \\ \mathbf{0} & \mathbf{R}_{\text{diag},i} \end{bmatrix} \mathbf{K}' \begin{bmatrix} \mathbf{R}_{\text{diag},i} & \mathbf{0} \\ \mathbf{0} & \mathbf{R}_{\text{diag},i} \end{bmatrix}^\top \quad (25)$$

The calculated stiffness \mathbf{K}_i is then used in the the impedance control (68) for the i -th fixture. In Section VIII-A, we show how this formulation creates a stiffness matrix with couplings between translational and rotational DoFs.

Please see Appendix B for the extension to manifolds \mathcal{M}_2 and \mathcal{M}_3 and Appendix C for an optimal damping calculation.

V. PROBABILISTIC DYNAMICAL SYSTEM VIRTUAL FIXTURES

We introduce automated DS based VFs which model the relationship between assistive velocities $\dot{\mathbf{x}}_{\text{DS}}$ and the current robot state \mathbf{x}_{ee} probabilistically, i.e.

$$p(\dot{\mathbf{x}}_{\text{DS}}|\mathbf{x}_{\text{ee}}) = \mathcal{N}(\dot{\mathbf{x}}_{\text{DS}}|\boldsymbol{\mu}_{\text{DS}}, \boldsymbol{\Sigma}_{\text{DS}}), \quad (26)$$

where $\boldsymbol{\mu}_{\text{DS}}$ denotes the mean of the dynamical system evaluated at \mathbf{x}_{ee} and $\boldsymbol{\Sigma}_{\text{DS}}$ the associated covariance. In contrast to time-driven motions, these models encode state-dependent dynamic behaviors that support user progression along the task, adapting their guidance with varying granularity – such as modulating velocity magnitude based on the task phase or enabling periodic motions. This distinguishes DS-based fixtures from the trajectory-based fixtures (Section VI) which can only encode a trajectory with start and end point. By providing motion information for the whole robot workspace, they are especially suited to the approaching phase of a manipulation where the robot may start at arbitrary configurations.

We adopt an uncertainty-aware, non-parametric approach that is highly flexible to composition and modulation without requiring parameter re-computation. Based on demonstration data, we use KMPs (Section III-C) to encode a specific task in a region of the workspace which results in N_{DS} concurrently active velocity fields on possibly different manifolds. In the following, $p_n(\dot{\mathbf{x}}_{\text{DS}})$ denotes the n -th of $N_{\text{DS}} - 1$ probabilistic DS models learned from demonstrations using KMPs (see Section V-A), and $p_{\text{stab}}(\dot{\mathbf{x}}_{\text{DS}})$ a probabilistic policy (see Section V-B) with a constant, pre-defined uncertainty that drives the robot toward the closest known dynamic. A proportional control scheme (Section V-C) allows us to use the learned dynamical system as probabilistic VFs. Through the arbitration scheme introduced in Section IV-A we leverage the epistemic uncertainty encoded by KMPs to automatically prioritize models with low uncertainty. When all models exhibit high uncertainty, the formulation defaults to the stabilizing policy $p_{\text{stab}}(\dot{\mathbf{x}})$ or to another type of fixtures, such as those introduced in Sections VI and VII.

A. Non-parametric Learning of Dynamical Systems

We define the n -th DS as a probabilistic mapping

$$p_n(\dot{\mathbf{x}}_{\text{DS}}|\mathbf{x}_{\text{ee}}) = \mathcal{N}(\dot{\mathbf{x}}_{\text{DS}}|\boldsymbol{\mu}_{\text{DS},n}, \boldsymbol{\Sigma}_{\text{DS},n}) \quad (27)$$

which can be learned from a dataset of demonstrations $\{\mathbf{x}_j, \dot{\mathbf{x}}_j\}_{j=1}^N$ where e.g. a full pose $\mathbf{x} \in \mathbf{R}^3 \times \mathcal{S}^3$ (\mathcal{M}_1) or only the position part $\mathbf{x} \in \mathbf{R}^3$ with velocities in the tangent

spaces $\dot{\mathbf{x}} \in \mathcal{T}_{\mathbf{x}}\mathcal{M}$ respectively $\dot{\mathbf{x}} \in \mathcal{T}_{\mathbf{x}}\mathbb{R}^3 = \mathbb{R}^3$ are used. This dataset is subsampled with equal spacing of the input poses to achieve a tradeoff between accuracy and computational cost.

The demonstrations are then used to learn a KMP (Section III-C). For the use in a DS, we deviate from the approach outlined therein for computing the reference distribution. First, we approximate the joint distribution between \mathbf{x} and $\dot{\mathbf{x}}$ in a GMM with M components and use GMR to compute the probabilistic reference velocities $\mathcal{N}(\dot{\mathbf{x}}_{\text{DS}}|\boldsymbol{\mu}_{\text{GMR}}, \boldsymbol{\Sigma}_{\text{GMR}})$. Through the averaging of the GMM, this results in a smooth velocity field. As the wrench calculated from this DS is later fused with wrenches from other VFs, we only use the velocity $\boldsymbol{\mu}_{\text{GMR}}$ resulting from the mixture regression. The covariance output $\boldsymbol{\Sigma}_{\text{GMR}}$ of the regression is discarded, as it would correspond to a covariance in velocity space which is not well suited for the fusion with fixtures with covariance in pose space. To obtain a better suiting covariance in pose space, we decompose datapoints $\boldsymbol{\xi}_j$ and the M Gaussians of the GMM into

$$\boldsymbol{\xi}_j = \begin{bmatrix} \mathbf{x}_j \\ \dot{\mathbf{x}}_j \end{bmatrix}, \quad \boldsymbol{\mu}_m = \begin{bmatrix} \boldsymbol{\mu}_m^I \\ \mathbf{0} \\ \boldsymbol{\mu}_m^I \end{bmatrix}, \quad \boldsymbol{\Sigma}_m = \begin{bmatrix} \boldsymbol{\Sigma}_m^I & \boldsymbol{\Sigma}_m^{IO} \\ \boldsymbol{\Sigma}_m^{OI} & \boldsymbol{\Sigma}_m^O \end{bmatrix} \quad (28)$$

which in turn allows to write a marginalized GMM using the weight factors π_m from the joint encoding (5)

$$p_n(\mathbf{x}) = \sum_{m=1}^M \pi_m \mathcal{N}(\mathbf{x}|\boldsymbol{\mu}_m^I, \boldsymbol{\Sigma}_m^I) \quad (29)$$

and to compute the likelihood of each Gaussian generating \mathbf{x}

$$e_m = \frac{\pi_m \mathcal{N}(\mathbf{x}|\boldsymbol{\mu}_m^I, \boldsymbol{\Sigma}_m^I)}{\sum_{m=1}^M \pi_m \mathcal{N}(\mathbf{x}|\boldsymbol{\mu}_m^I, \boldsymbol{\Sigma}_m^I)}. \quad (30)$$

Using those weighting factors, we compute $\hat{\boldsymbol{\Sigma}}$ through a unimodal approximation (7) of the GMM (29). This results in a probabilistic velocity field $\mathcal{N}(\boldsymbol{\mu}_{\text{GMR}}, \hat{\boldsymbol{\Sigma}})$. We sample this velocity field at a subsampled set of N_{ref} poses from the demonstrated trajectories to obtain a probabilistic reference $\{\boldsymbol{\mu}_{\text{GMR},n}, \hat{\boldsymbol{\Sigma}}_n\}_{n=1}^{N_{\text{ref}}}$ which is then encoded into the KMP. Finally, KMP mean and covariance predictions (8), (9) provide $\boldsymbol{\mu}_{\text{DS}}, \boldsymbol{\Sigma}_{\text{DS}}$ in (27) at each end effector pose \mathbf{x}_{ee} .

We propose to use an on-manifold kernel as covariance function in our experiments. Particularly we use the Radial Basis Function (RBF) kernel with the distance function (2)

$$k(\mathbf{x}, \mathbf{x}_{\text{ee}}) = \exp\left(-\frac{d_{\mathbf{I}}^M(\mathbf{x}, \mathbf{x}_{\text{ee}})}{2l^2}\right), \quad (31)$$

where l denotes the length scale. Similarly to GPs, we assume a zero-mean prior, so predictions from (8) yield $\dot{\mathbf{x}}_{\text{DS}} = \mathbf{0}$ in regions far from the demonstrations. Moreover, (9) captures aleatoric uncertainty near the data and reflects increasing epistemic uncertainty in regions with limited or no demonstrations. Note that the distance function in (31) naturally extends to the manifold \mathcal{M} chosen for the task. We treat the output as Euclidean, therefore, only the kernel has to be adapted to the manifold case assuming that the learned velocities are smooth and the length scale parameter of the kernel is small compared to the changes of the velocity.

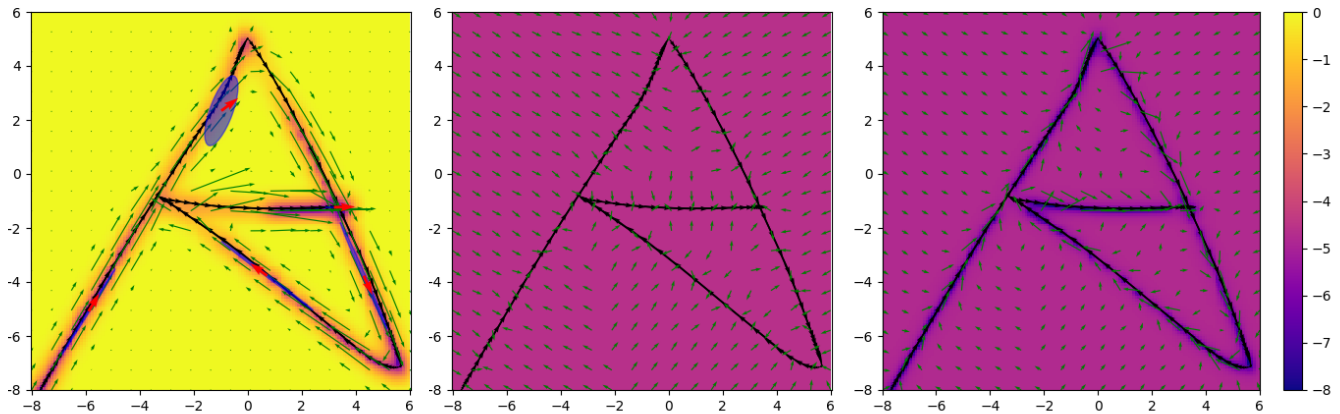


Fig. 4: 2D motion policy learned using a KMP. Black arrows depict the velocity profile from the training data, an “A” from the letter dataset [59]. The left image shows the output of the KMP (Section V-A) at rastered locations, blue ellipsoids and red arrows depict centers, position covariances and velocities of the Gaussians of the GMM used to learn the KMP. The middle image shows the probabilistic base policy (Section V-B) and the right image the final velocities resulting from the arbitration. The colormap of each plot depicts $\log(\det(\Sigma))$.

B. Probabilistic Stabilizing Policy

Outside of the task space regions where demonstrations were provided, the robot actions computed from (27) are zero, rendering the resulting velocity fields invalid. A probabilistic *stabilizing policy*²

$$p_{\text{stab}}(\dot{\mathbf{x}}_{\text{DS}}|\mathbf{x}_{\text{ee}}) = \mathcal{N}(\dot{\mathbf{x}}_{\text{DS}}|\boldsymbol{\mu}_{\text{stab}}, \boldsymbol{\Sigma}_{\text{stab}}), \quad (32)$$

which brings the robot back into the demonstrated areas, is therefore necessary. To achieve this, we compute the distance to the reference poses of all N_{DS} velocity fields using (2) to $d_j = d_{\mathcal{I}}^{\mathcal{M}_1}(\mathbf{x}_j, \mathbf{x}_{\text{ee}})$ and obtain the closest pose \mathbf{x}_{j^*} of a known dynamic with

$$j^* = \underset{j}{\operatorname{argmin}} d_j. \quad (33)$$

We then calculate a normalized velocity $\boldsymbol{\mu}_{\text{stab}}$ in direction of this closest pose

$$\boldsymbol{\mu}_{\text{stab}} = \dot{\mathbf{x}}_0 \frac{\operatorname{Log}_{\mathbf{x}_{\text{ee}}}^{\mathcal{M}_1}(\mathbf{x}_{j^*})}{\sqrt{d_{\mathcal{I}}^{\mathcal{M}}(\mathbf{x}_{\text{ee}}, \mathbf{x}_{j^*})}} \quad (34)$$

using the on-manifold distance function (2) and a default velocity $\dot{\mathbf{x}}_0$ which is then equipped with a constant covariance

$$\boldsymbol{\Sigma}_{\text{stab}} = \sigma_{\text{stab}} \mathbf{I}_6. \quad (35)$$

The covariance σ_{stab} of this policy is an important hyperparameter – it has to be chosen such that $\boldsymbol{\Sigma}_{\text{stab}}$ is bigger than the covariances $\boldsymbol{\Sigma}_{\text{DS},n}$ of the learned DSs in the areas where demonstrations have been provided. Thanks to KMPs providing epistemic uncertainty, the covariances $\boldsymbol{\Sigma}_{\text{DS},n}$ increase outside of the demonstrated areas, therefore activating the stabilizing policy which brings the robot back inside the demonstrated areas through the arbitration (16).

Fig. 4 shows a DS learned using our approach on 2D data [59]. For this example, we use a RBF kernel with length scale $l = 0.3$, the KMP is initialized from a GMM with 5 Gaussians sampled at the location of the input data and base policy with $\boldsymbol{\Sigma} = \operatorname{diag}(0.1, 0.1)$. We show the advantages of such KMP-based policy over GPs in Section VIII-C.

²This policy is not stabilizing in a sense of ensuring convergence but a *soft* stability bringing the robot back to regions of learned DSs.

C. Control Law for DS-based Virtual Fixtures

In order to use velocity fields as VFs, we use a proportional control law computing the mean wrenches $\mathbf{w}_{\text{VF},i}$ as

$$\mathbf{w}_{\text{VF},i} = \mathbf{D}_{\text{VF},i}(\dot{\mathbf{x}}_{\text{VF},i} - \dot{\mathbf{x}}_{\text{ee}}) \quad (36)$$

with the end effector velocity $\dot{\mathbf{x}}_{\text{ee}}$, VF velocity $\dot{\mathbf{x}}_{\text{VF},i}$ ($\boldsymbol{\mu}_{\text{DS}}$ from (26)) both expressed in the tangent space $\mathcal{T}_{\mathbf{x}_{\text{ee}}}\mathcal{M}$ and the constant damping matrix $\mathbf{D}_{\text{VF},i}$. Note that (36) can be derived from (4) by setting $\mathbf{K}_{\text{VF},i} = \mathbf{0}$.

Note that $\mathbf{w}_{\text{VF},i}$ is expressed in the cotangent space $\mathcal{T}_{\mathbf{x}_{\text{ee}}}^*\mathcal{M}$. As detailed in Section IV-A, $\mathbf{w}_{\text{VF},i}$ and the associated covariance $\boldsymbol{\Sigma}_{\text{VF},i}$ have to be transformed to the (co)tangent space of $\mathbb{R}^3 \times \mathcal{S}^3$ which allows for a natural arbitration between different velocity fixtures and other types of VFs.

VI. POSITION-BASED TRAJECTORY FIXTURES: LEARNING, ARBITRATION AND AUTOMATION

In contrast to DS based VFs (Section V), position-based trajectories output a probabilistic attractor pose

$$p(\mathbf{x}_{\text{PB}}|\mathbf{x}_{\text{ee}}) = \mathcal{N}(\mathbf{x}_{\text{PB}}|\boldsymbol{\mu}_{\text{PB}}, \boldsymbol{\Sigma}_{\text{PB}}) \quad (37)$$

which is then applied to the robot using impedance control with variable stiffness (Section IV-B). This formulation requires both a probabilistic trajectory as well as a distance function for mapping the robot end effector pose \mathbf{x}_{ee} to the closest pose on the trajectory. To benefit from the different manifolds \mathcal{M} introduced in Section III-A, we show the extension of [8] from the manifold $\mathbb{R}^3 \times \mathcal{S}^3$ to \mathcal{M} . Furthermore, we introduce an automation of this fixture in Section VI-D. In our approach, we consider N_{PB} concurrently active trajectory fixtures.

A. Learning of Trajectory Fixtures on different Manifolds \mathcal{M}

We assume to have access to a dataset of trajectories $\{t_i, \mathbf{x}_i\}_{i=1}^N$ from demonstrations with time $t \in \mathbb{R}^1$ and pose $\mathbf{x} \in \mathcal{M}$ for each of the N_{PB} fixtures. We rely on dynamic time warping (DTW) [61] for aligning the individual demonstrations in $t \in [0, 1]$ to encode them in a GMM (5) with M components.

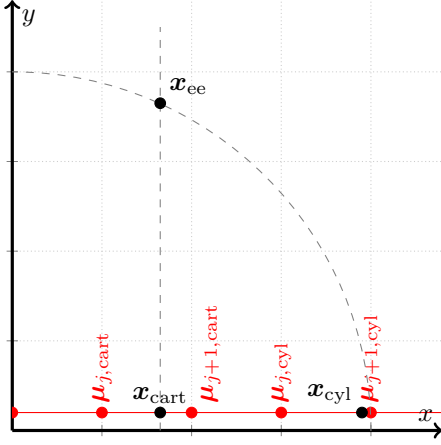


Fig. 5: 2D projection of \mathbf{x}_{ee} and the closest poses μ_j and μ_{j+1} on a trajectory (red points) in $\mathbb{R}^3 \times \mathcal{S}^3$ (\mathbf{x}_{cart}) as well as $\mathcal{S}^1 \times \mathbb{R}^2 \times \mathcal{S}^3$ (\mathbf{x}_{cyl}). The x axis through \mathbf{x}_{ee} as well as the circle with the same radius on $\mathcal{S}^1 \times \mathbb{R}^2 \times \mathcal{S}^3$ is plotted in dashed gray, note that according to the manifold metric the closest pose is much further to the right than for Cartesian coordinates.

To benefit from the properties of different manifolds \mathcal{M} , we use the square root of the distance function defined in (2) with $\mathbf{A} = \mathbf{I}$ as distance measure between the two poses \mathbf{x}_j and \mathbf{x}_k in the DTW calculation. This for example allows us to learn trajectories in cylindrical coordinates \mathcal{M}_2 , see Section VIII-D for evaluation details. The effect of this distance measure for Cartesian and cylindrical coordinate systems is shown in Fig. 5. The result of this DTW operation is comparable to the introduction of a phase variable [22].

Using GMR, we condition the GMM on time t to obtain probabilistic poses $p(\mathbf{x}|t)$ (6). Section VI-B details how a single attractor can be computed from such time-based probabilistic trajectory which is then used in an on-manifold impedance controller (4) with variable stiffness (Section IV-B).

B. On-Manifold Attractor Point Calculation

For impedance control, a single attractor point as in (7) is needed. In the Euclidean case, a closed form solution exists for extracting this point on a time-based probabilistic trajectory [21]. As on-manifold Gaussian operations require iterations with a variable number of steps [47], they are not well suited for real-time control. We therefore extract a trajectory from the conditional distribution $p(\mathbf{x}|t)$ by calculating $\{\mu_n, \Sigma_n\}_{n=1}^N$ for N equally spaced samples of $t \in [0, 1]$. This trajectory is then sent to the real-time controller for interpolation.

In the real-time controller, the two closest poses μ_j and μ_{j+1} of this trajectory according to the on-manifold Mahalanobis distance $d_{\Sigma_j}^{\mathcal{M}}(\mu_n, \mathbf{x}_{ee})$ (2) are extracted. For simplicity we use only the position part of the pose in the distance function, where we set the last three entries of μ_j and \mathbf{x}_{ee} , which correspond to the orientation, to the identity. We then perform linear interpolation between both extracted poses along the covariance-deformed geodesic on the manifold

(Fig. 5), using

$$\begin{aligned} \Delta\mu_{j,j+1} &= \text{Log}_{\mu_j}^{\mathcal{M}} \mu_{j+1}, & \Delta\mu_{j,ee} &= \text{Log}_{\mu_j}^{\mathcal{M}} \mathbf{x}_{ee}, & (38) \\ \nu &= \frac{\Delta\mu_{j,ee}^{\top} \Sigma_j^{-1} \Delta\mu_{j,j+1}}{\Delta\mu_{j,j+1}^{\top} \Sigma_j^{-1} \Delta\mu_{j,j+1}}, & \mathbf{x}_{\text{PB}} &= \text{Exp}_{\mu_j}^{\mathcal{M}} (\nu \cdot \Delta\mu_{j,j+1}) & (39) \end{aligned}$$

where $\Delta\mu_{j,j+1}$ is the vector between μ_j and μ_{j+1} and $\Delta\mu_{j,ee}$ between μ_j and \mathbf{x}_{ee} in tangent space and Σ_j^{-1} the precision matrix corresponding to μ_j . The interpolation factor $0 \leq \nu \leq 1$ represents the closeness of \mathbf{x}_{ee} to μ_j and μ_{j+1} and \mathbf{x}_{VF} the final VF pose which is used in (4) to calculate the wrench $\mathbf{w}_{\text{VF},i}$ associated to the fixture. Its computation through (39) takes the Mahalanobis distance between the end effector and the two closest means into account. As we assume the covariance matrix to only vary slowly between points we set $\Sigma_{\text{PB}} = \Sigma_j$ which is associated with μ_j , however, interpolation could be performed similarly on the manifold of symmetric positive definite matrices [48].

The manifold-aware attractor calculation through (38) and (39) ensures that only forces orthogonal to the trajectory are being applied by the fixture and thus the user is in full control of motion along to the trajectory.

C. Distance-based Covariance Adaptation

The covariance matrix Σ_{PB} is used for subsequent variable impedance control (Section IV-B) and for the arbitration with other fixtures (IV-A). By default, the covariance matrix only depends on the closest point of the trajectory, thus only modeling aleatoric uncertainty, and does not incorporate the end effector distance to the trajectory. This results in large wrenches \mathbf{w}_{PB} when the end effector \mathbf{x}_{ee} is far away from the fixture even though the trajectory might not be valid anymore for the current robot pose. We therefore propose to adapt the original covariance output of the fixture by a linear distance-based scaling of the precision matrix $\mathbf{P}_{\text{PB}} = \Sigma_{\text{PB}}^{-1}$

$$\hat{\mathbf{P}}_{\text{PB}} = s \cdot \mathbf{P}_{\text{PB}} \quad (40)$$

using

$$s = \begin{cases} 1, & d < d_{\min} \\ 1 - \frac{d_{\mathcal{M}}^{\mathcal{P}_{\text{PB}}}(\mathbf{x}_{\text{PB}}, \mathbf{x}_{ee}) - d_{\min}}{d_{\max} - d_{\min}}, & d_{\min} \leq d \leq d_{\max} \\ 0, & d > d_{\max} \end{cases} \quad (41)$$

with the Mahalanobis distance $d_{\mathcal{M}}^{\mathcal{P}_{\text{PB}}}(\mathbf{x}_{\text{PB}}, \mathbf{x}_{ee})$ between end effector \mathbf{x}_{ee} and fixture attractor \mathbf{x}_{PB} weighted by the precision matrix \mathbf{P}_{PB} . The parameters d_{\min} and d_{\max} determine the distances at which the precision matrix scaling starts and ends, respectively. Using the Mahalanobis distance takes the influence of specific DoFs into account, thus leaving the fixture active for longer in directions with high uncertainty. This is relevant to exploit the variable stiffness formulation (Section IV-B) where those directions get much lower stiffnesses, thus allowing the operator to move more freely. The resulting behaviour is showcased in Section VIII-G.

D. Automating the Fixture

As the position-based fixture is derived from a time-driven motion, we can compute a preferred direction along the trajectory. Inspired by [36], we calculate the current direction

$$\delta = \boldsymbol{\mu}_{j+1,\text{pos}} - \boldsymbol{\mu}_{j,\text{pos}} \quad (42)$$

where $\boldsymbol{\mu}_{j,\text{pos}}$ and $\boldsymbol{\mu}_{j+1,\text{pos}}$ are the \mathbb{R}^3 positions of the interpolation points of the fixture. Subsequently, we normalize δ to $\tilde{\delta} = \frac{\delta}{\|\delta\|}$. The same velocity controller as employed for DS based fixtures (Section V-C) is used to calculate an automation wrench $\mathbf{w}_{\text{VF},\text{aut},i}$ from $\tilde{\delta}$. The resulting wrench is then added to the wrench coming from the impedance controller (4)

$$\tilde{\mathbf{w}}_{\text{VF},i} = \mathbf{w}_{\text{VF},i} + \mathbf{w}_{\text{VF},\text{aut},i}. \quad (43)$$

Finally, the wrenches $\tilde{\mathbf{w}}_{\text{VF},i}$ of all N_{PB} trajectory fixtures are arbitrated with the other fixture types through (16).

VII. GEOMETRIC VISUAL SERVOING FIXTURE

Probabilistic visual servoing VFs as introduced in [8] model the attractor point of a fixture based on visual input I

$$p(\mathbf{x}_{\text{VS}}|\text{I}) = \mathcal{N}(\mathbf{x}_{\text{VS}}|\boldsymbol{\mu}_{\text{VS}}, \boldsymbol{\Sigma}_{\text{VS}}). \quad (44)$$

We consider N_{VS} concurrently active visual servoing VFs, each modeling the combination of M individual fixtures, one for every visual detection $p_m(\mathbf{x}_{\text{VS}}|\mathbf{x}_{\text{ee}}) = \mathcal{N}(\mathbf{x}_{\text{VS}}|\boldsymbol{\mu}_m, \boldsymbol{\Sigma}_m)$, depending on the end effector pose \mathbf{x}_{ee} . A MoE model [51], [62] allows to model the fixture as a multi-modal distribution

$$p(\mathbf{x}_{\text{VS}}|\mathbf{x}_{\text{ee}}) = \sum_{m=1}^M \hat{h}_m(\mathbf{x}_{\text{ee}}, \boldsymbol{\mu}_m) p_m(\mathbf{x}_{\text{VS}}|\mathbf{x}_{\text{ee}}). \quad (45)$$

A. Geometry-aware Mixture of Experts Gating Functions

In [63], the *gating function* h_m computes the influence of each expert based on the distance between expert and end effector poses in $\mathbb{R}^3 \times \mathcal{S}^3$. Here, we introduce a generalized formulation for the manifolds defined in Section III-A. Leveraging the geometry-aware distance function (2), we have

$$h_m(\mathbf{x}_{\text{ee}}, \boldsymbol{\mu}_m) = \exp\left(-\frac{1}{2}d_{\mathbf{L}}^{\mathcal{M}}(\mathbf{x}_{\text{ee}}, \boldsymbol{\mu}_m)\right) + \gamma \quad (46)$$

where γ is a regularization factor and the hyperparameter $\mathbf{L} = \text{diag}(l_0^2, l_1^2, l_2^2, l_{wx}^2, l_{wy}^2, l_{wz}^2)^{-1}$ allows to specify the relevance of each direction. For the \mathcal{M}_1 , l_0 , l_1 and l_2 correspond to x , y and z . For \mathcal{M}_2 , l_0 and l_1 instead correspond to the angular DoF and the radius r . In case of \mathcal{M}_3 , l_0 and l_1 weigh the two angular DoFs and l_2 the radius r .

When far from all detections, γ assigns equal weights for each expert, reflecting the overall uncertainty of all detections. Similarly to [8] we compute a unimodal distribution from (45) via moment matching resulting in mean $\boldsymbol{\mu}_{\text{VS}}$ and covariance $\boldsymbol{\Sigma}_{\text{VS}}$, used by the impedance controller (4). The variable stiffness formulation introduced in Section IV-B, in contrast to [8], also allows to model off-diagonal stiffness directions as well as couplings between positional and rotational DoFs. This e.g. permits to render the transition between detections with different orientations as shown in Section VIII-A. Arbitration with other fixtures is again performed using (16).

B. Geometric Expert Customization

While the *gating function* h_m of [8] naturally extends to other manifolds, the expert customization also found therein needs to be flexibilised and formalized.

1) *Zero force along insertion axis*: We assume that the insertion that should be controlled by the operator is to be performed along one DoF of the chosen manifold. Therefore, the stiffness in the corresponding row of \mathbf{K} is set to zero to not generate any forces along this axis and allow the operator full control over the insertion.

2) *Deadzones*: In the vicinity of a connector, the operator should receive strong guidance. This can be achieved by modifying $\text{Log}_{\mathbf{x}_{\text{ee}}}^{\mathcal{M}}(\boldsymbol{\mu}_m)$, setting its entries to zero for distances smaller than a predefined radius and scaling it for larger distances. To flexibly parameterize these differences, we use a length vector \mathbf{l}_{dead} to deform the difference vector as well as the scalar deadzone value r_{dead} . Using those parameters, we calculate $\text{Log}_{\mathbf{x}_{\text{ee}}}^{\mathcal{M}}(\boldsymbol{\mu}_m)$ from $\text{Log}_{\mathbf{x}_{\text{ee}}}^{\mathcal{M}}(\boldsymbol{\mu}_m)$ as follows:

$$\mathbf{L}_{\text{dead}} = \text{diag}(\mathbf{l}_{\text{dead}}^{-2}) \quad (47)$$

$$r = \sqrt{d_{\mathbf{L}_{\text{dead}}}^{\mathcal{M}}(\mathbf{x}_{\text{ee}}, \boldsymbol{\mu}_m)} \quad (48)$$

$$\mathbf{d} = \frac{\text{Log}_{\mathbf{x}_{\text{ee}}}^{\mathcal{M}}(\boldsymbol{\mu}_m)}{r} \quad (49)$$

$$r_{\text{crop}} = \min(r, r_{\text{dead}}) \quad (50)$$

$$d'_j = \begin{cases} d_j, & l_{\text{dead},j} > 0 \\ 0, & l_{\text{dead},j} = 0 \end{cases} \quad (51)$$

$$\text{Log}_{\mathbf{x}_{\text{ee}}}^{\mathcal{M}}(\boldsymbol{\mu}_m) = \text{Log}_{\mathbf{x}_{\text{ee}}}^{\mathcal{M}}(\boldsymbol{\mu}_m) - r_{\text{crop}} \cdot \mathbf{d}' \quad (52)$$

(48) uses the on-manifold distance (2), (51) ensures that only directions with length vector > 0 get modified. The modified value $\text{Log}_{\mathbf{x}_{\text{ee}}}^{\mathcal{M}}(\boldsymbol{\mu}_m)$ is then used in the gating function (46).

3) *Expert Initialization*: As in [8], we initialize the MoE with an additional expert at the end effector pose with high covariance. This additional expert ensures that the fixture does not generate forces outside its valid region. It is parameterized with length scale $\mathbf{l}_{\text{dead,add}}$ and dead zone $r_{\text{dead,add}}$, calculating the modified difference $\text{Log}_{\mathbf{x}_{\text{ee}}}^{\mathcal{M}}(\boldsymbol{\mu}_m)$ using (47) through (52). Its influence factor h_{M+1} is then calculated as in [8]

$$h_{M+1}(\mathbf{x}_{\text{ee}}, \mathbf{x}_{\text{targ}}) = 1 - \exp\left(-\frac{1}{2}d_{\mathbf{L}_{\text{add}}}^{\mathcal{M}}(\mathbf{x}_{\text{ee}}, \boldsymbol{\mu}_m)\right), \quad (53)$$

where $\mathbf{L}_{\text{add}} = \text{diag}(\mathbf{l}_{\text{add}})$ is the length vector for the additional expert, \mathbf{x}_{targ} the expected mean of the visual servoing experts and the modified logarithmic map from (52) is again used in the distance calculation.

VIII. EVALUATION

For evaluating the method, we have implemented the framework on three different robotic systems (Fig. 6). First, we use a torque-controlled 7-DoF manipulator where fixtures are integrated into the real-time controller, rendering forces at 8 kHz. We use this robot in hand-guided mode, i.e. an operator directly interacts with the robot arm where the fixtures are rendered. A space-ready, 4-DoF robot arm mounted on a base plate with various interaction elements is used as second



Fig. 6: Overview of the robotic systems used for the evaluation. A torque-controlled 7-DoF manipulator shown in the leftmost image is used in hand-guided mode, where the operator directly interacts with the robot. It is used for evaluating individual fixtures in Sections VIII-A to VIII-C as well as their combinations in Sections VIII-F and VIII-G. The middle image depicts a space-ready, 4-DoF robot arm which is used with fully automated fixtures only. It is used for evaluation in Sections VIII-C to VIII-E. The rightmost image shows a bilateral teleoperation setup with two torque-controlled 7-DoF manipulators which is used for evaluating the fixtures in a teleoperation task in Section VIII-F.

system. This setup is meant to be tested in outer space. As preparatory experiment, we have evaluated our methods in weightlessness on a parabolic flight. During the flight no direct interaction with the robot was possible and no haptic device was coupled to it. Thus, we tested all fixtures on the system in fully automated mode. Only the position of the robot was controlled to allow for a one DoF nullspace of the robot. Third system was a bilateral teleoperation setup with two torque-controlled 7-DoF manipulators where one robot arm was used as haptic input device and the other arm as remote robot to test the fixtures in a teleoperation setup. All fixtures are arbitrated through (16) and applied to the robot using (3).

We first start by a componentwise evaluation of the individual fixtures, beginning with the visual servoing fixture with variable stiffness in Section VIII-A. In this experiment, we exploit that our variable stiffness formulation allows for couplings between translational and rotational DoFs. Next, we evaluate the position-based fixture on a spherical manifold in Section VIII-B showcasing the on-manifold attractor point calculation (VI-B) combined with variable stiffness for a pointing task. We then focus on the novel dynamical system VFs in Section VIII-C. Finally, we evaluate the automated position-based fixture (Section VIII-D).

As our framework supports the probabilistic fusion of VFs, we then evaluate multiple fixture combinations. We evaluate the combination of dynamical system and position-based fixtures (Section VIII-E) as well as of dynamical system and visual servoing fixtures (Section VIII-F). Finally, we show a combination of the full set of fixtures (Section VIII-G).

A. Visual Servoing Fixture with Coupled Variable Stiffness

Section IV-B introduces a variable stiffness formulation taking full 6×6 covariance matrices into account. Such matrices with couplings between translational and rotational DoFs can e.g. result from the MoE formulation of the Visual Servoing Fixture (Section VII) when two neighbouring detections have different orientations. Figure 7 shows the result of this algorithm on the use case of robotic chess playing on a torque-controlled 7-DoF manipulator in hand-guided operation, where two chess figures with different orientation can be grasped. Simulated visual detections on the fields 1a and 8h ($N_{VS} = 1$, $M = 2$) with covariance $\Sigma = 5 \times 10^{-6} \cdot \mathbf{I}_6$ on a chess field with size of $40 \text{ cm} \times 40 \text{ cm}$ and parameters

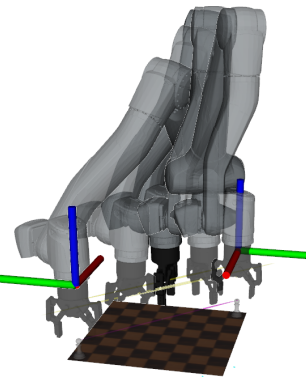


Fig. 7: Visual servoing fixture (Section VII) on \mathcal{M}_1 with two targets with an orientation difference of 180° around the z axis and position differences both along the x and y axis. This leads to a covariance matrix with couplings both inside the positional as well as between positional and rotational DoFs, therefore necessitating a fully populated stiffness matrix.

$l_x = l_y = l_z = 0.06$, $l_{wx} = l_{wy} = l_{wz} = 0.2$, $\gamma = 1 \times 10^{-20}$ leads to an in-between attractor point with the precision matrix

$$\mathbf{P} = \begin{bmatrix} 2.0 \times 10^5 & 2.3 \times 10^3 & -1.8 \times 10^1 & 1.4 \times 10^{-1} & -1.4 \times 10^{-1} & -2.2 \times 10^4 \\ 2.4 \times 10^3 & 2.0 \times 10^5 & 1.8 \times 10^1 & -1.4 \times 10^{-1} & 1.4 \times 10^{-1} & 2.2 \times 10^4 \\ -1.8 \times 10^1 & 1.8 \times 10^1 & 2.0 \times 10^5 & 1.0 \times 10^{-3} & -1.0 \times 10^{-3} & -1.6 \times 10^2 \\ 1.4 \times 10^{-1} & -1.4 \times 10^{-1} & 1.0 \times 10^{-3} & 2.0 \times 10^5 & -4.0 & 1.2 \\ -1.4 \times 10^{-1} & 1.4 \times 10^{-1} & -1.0 \times 10^{-3} & -4.0 & 2.0 \times 10^5 & -1.3 \\ -2.2 \times 10^4 & 2.2 \times 10^4 & -1.6 \times 10^2 & 1.2 & -1.3 & 4.8 \times 10^3 \end{bmatrix}. \quad (54)$$

The variable stiffness formulation (Section IV-B) with $\lambda_{\text{rot}}^- = \lambda_{\text{trans}}^- = 1000$, $\lambda_{\text{rot}}^+ = \lambda_{\text{trans}}^+ = 2500$, $k_{\text{trans,nom}} = 1000$ and $k_{\text{rot,nom}} = 40$ computes the coupled stiffness matrix

$$\mathbf{K} = \begin{bmatrix} 1000.0 & * & * & * & * & -111.4 \\ * & 1000.0 & * & * & * & 111.5 \\ * & * & 1000.0 & * & * & -0.8 \\ * & * & * & 40.0 & * & * \\ * & * & * & * & 40.0 & * \\ -111.4 & 111.5 & -0.8 & * & * & 24.8 \end{bmatrix}, \quad (55)$$

with entries $* < 1e-3$, allowing the operator to freely move along the geodesic between both detections. This geodesic couples translational movement with an orientation change as can be seen in Fig. 7 as well as in the accompanying video and is further discussed in Section IX-C. Note that along this geodesic, unlike in [8], the operator is not always attracted to one of the simulated detections as the choice of length scales assigns approximately equal weights to both detections when the end effector is located between them.

B. Position-based Fixture with Variable Stiffness

The variable stiffness formulation (Section IV-B) is also well suited for spherical manifolds $\mathcal{S}^2 \times \mathbb{R}^1 \times \mathcal{S}^3$. From only four demonstrations of a movement towards the origin of the spherical coordinate system \mathcal{M}_3 , we are able to learn a trajectory fixture ($N_{\text{PB}} = 1$) supported by $M = 2$ Gaussians as visualized in Fig. 8. The resulting fixture exhibits a large covariance around the two rotational DoFs of \mathcal{S}^2 as can be seen by the turquoise Gaussian visible behind the robot's end effector as well as from the precision matrix with relatively small entries $P_{1,1}$, $P_{2,2}$ and $P_{3,3}$

$$\mathbf{P} = \begin{bmatrix} 344 & -23 & -109 & -110 & 280 & -166 \\ -23 & 46 & 58 & 133 & 48 & 31 \\ -109 & 58 & 723 & -74 & -22 & 78 \\ -110 & 133 & -74 & 794 & 58 & 112 \\ 280 & 48 & -22 & 58 & 533 & -81 \\ -166 & 31 & 78 & 112 & -81 & 94 \end{bmatrix}. \quad (56)$$

With $\lambda_{\text{rot}}^- = 0.5$, $\lambda_{\text{rot}}^+ = 1.5$, $\lambda_{\text{trans}}^- = 400$, $\lambda_{\text{trans}}^+ = 500$, $k_{\text{trans,nom}} = 500$ and $k_{\text{rot,nom}} = 40$, the stiffness matrix

$$\mathbf{K} = \begin{bmatrix} 5 & -2 & -20 & * & 2 & -3 \\ -2 & * & 7 & * & * & 1 \\ -20 & 7 & 74 & -3 & -9 & 12 \\ * & * & -3 & 40 & * & * \\ 2 & * & -9 & * & 41 & -1 \\ -3 & 1 & 12 & * & -2 & 42 \end{bmatrix} \quad (57)$$

with entries $* < 1$ results, which has much scaled-down values compared to the nominal stiffness matrix $\mathbf{K}_{\text{nom}} = \text{diag}(80, 80, 500, 40, 40, 40)$ at $r = 16$ cm. Therefore, the fixture allows a human operator to freely move around the object centered at the coordinate origin while always pointing at it which is e.g. valuable for inspection tasks.

Crucial for this fixture is also the correct attractor point selection through (38), (39). It ensures that the attractor point stays the same when moving along a zero-force direction extracted by the variable impedance control Section IV-B. This is achieved by computing both attractor point as well as stiffness from the precision matrix $\mathbf{P}_{\text{VF}} = \Sigma_{\text{VF}}^{-1}$, ensuring that length scales in the distance calculation correspond to stiffness scales. The difference between attractor points computed through this weighted as well as a non-weighted formulation can clearly be seen in Fig. 8, highlighting the importance of this formulation as the attractor point computed without weighting would result in forces along the trajectory. Please see the supplementary video for details on how the fixture allows a human operator to move the robot in hand-guided mode.

C. Probabilistic Dynamical System Virtual Fixtures

To evaluate the novel dynamical system VF (Section V), we demonstrate two transport motions from right to left in the robot's workspace (Figs. 9 and 10). The right motion consists of five demonstrations diverging towards the middle of the workspace while the left motion consists of four demonstrations which are very close together. For evaluation purposes we compare the performance of GP and KMP representations on \mathcal{M}_1 . To limit the amount of data used in the models, the recorded trajectories are subsampled at a distance of 5 cm before calculating the velocities based on time differences.

Through empirical trials we have found that with human interaction, encoding velocity policies using a full pose $\mathbf{x} \in \mathcal{M}$

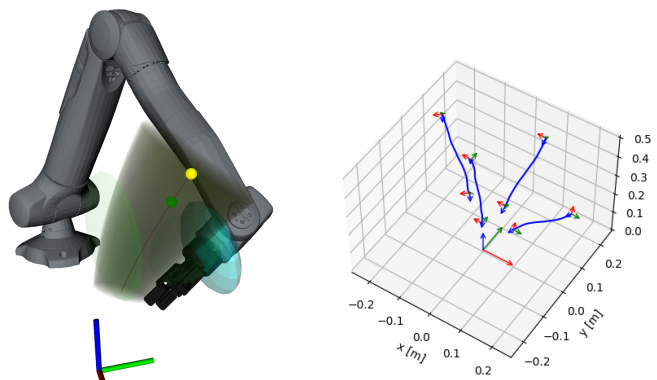


Fig. 8: Position-based fixture (Section VI) on the spherical manifold \mathcal{M}_3 ($\mathcal{S}^2 \times \mathbb{R}^1 \times \mathcal{S}^3$) with variable stiffness learned from four demonstrations (right side). The trajectory with red mean and covariance visualized as yellow tube consists of $M = 2$ Gaussians plotted as green ellipsoids. The task exhibits a high variance along the two angular DoFs of the spherical manifold as visualized by the turquoise ellipsoid at the end effector; a corresponding low stiffness allows the operator to point to an object located at the center of the coordinate system from any angle. The green dot on the red mean trajectory depicts the attractor point computed using the Mahalanobis distance ($\mathbf{A} = \Sigma^{-1}$ in (2)) while the yellow dot would be computed using a non-weighted distance metric ($\mathbf{A} = \mathbf{I}$ in (2)).

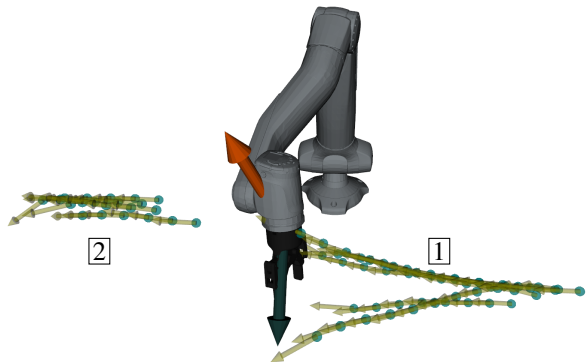


Fig. 9: DS based VF using a GP model. Turquoise dots represent points of known velocities visualized by yellow arrows. The green arrow corresponds to the output of the velocity policy [1] on the right side while the red arrow depicts the velocity output of the velocity policy [2]. Both counteract each other due to erroneous velocity measurements at the borders of the dataset, leading to a stuck evolution of the system unable to transition from [1] to [2].

as input and outputting a velocity $\dot{\mathbf{x}} \in \mathbb{R}^6$ leads to non-smooth behaviour due to the curse of dimensionality. When a human interacts with the robot and perturbs its orientation, the epistemic uncertainty of the velocity policy increases, activating the base policy. The base policy only pulls the operator to the closest known pose \mathbf{x} without the forward motion component $\dot{\mathbf{x}}$, therefore halting the evolution of the DS. Splitting the DS in two components, one with position input $\mathbf{x}_{\text{pos}} \in \mathbb{R}^3$ and output velocity $\dot{\mathbf{x}}_{\text{pos}} \in \mathbb{R}^3$ and the other with the full pose as input $\mathbf{x} \in \mathcal{M}$ and rotational velocity $\boldsymbol{\omega} \in \mathcal{T}_{\mathbf{x}_{\text{rot}}}^{\mathcal{S}^3}$ as output, this problem can be mitigated. The full set of velocity policies for this experiment therefore consists of $N_{\text{DS}} = 5$ concurrently active policies: one base policy and two policies each for the left and the right side of the motion. All policies are fused through the arbitration in (16).

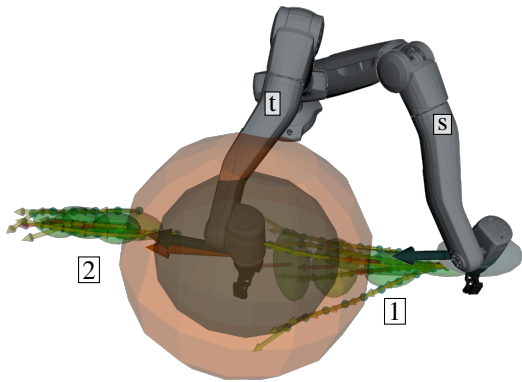


Fig. 10: DS-based VF using a KMP model for the robot in start [S] and transition [T] configurations. As in Fig. 9, turquoise dots represent points of known velocities visualized by yellow arrows. The positional uncertainty of the GMM underlying the KMP model is visualized as green Gaussians with their velocity as red arrows. The dark green Gaussian with green velocity arrow at the end effector represents the covariance output of the KMP [1]. The orange-red Gaussian with red velocity arrow at the end effector visible for the [T] configuration corresponds to the velocity policy [2]. In [T], a smooth transition between both policies is happening. In the [S] configuration, no output for policy [1] is visible due to its high uncertainty.

In Fig. 9, velocity policies encoded using a GP are visualized. For the positional GP we use a RBF kernel (31) with $l = 0.1$ and for the rotational GP $l = 0.03$. We set the process variance for both to $\lambda = 0.01$. As shown in the supplementary video, the evolution of the DS closely follows the demonstration trajectories but fails to capture their variance, both for the left and right side policies. Furthermore, the velocities generated by the GP encoding, as seen in Fig. 11, exhibit abrupt changes, suggesting limited smoothness in the generated trajectories. A higher value of λ could smoothen the prediction of the process output, which would however have a global effect and not be restricted to the demonstrated high-variance zone. The robot also fails to transition between policies, halting at the final pose of the rightmost demonstrations and requiring operator input to proceed.

Fig. 10 shows the same data encoded in a DS using a KMP based on a GMM with $M = 5$ Gaussians with hyperparameters $\lambda = 0.05$, $\lambda_c = 10$, $\alpha = 0.1$ and $l = 0.1$ in the RBF kernel for the positional KMP respectively $l = 0.03$ for the rotational KMP. The KMP allows to encode a small start covariance at [S] configuration and a bigger end covariance at [T] configuration for the right motion policy. This also enables a system evolution across the gap from the right to the left policy where the GP-based policy halted. Unlike the previous model, the learned covariance permits smoother motion in the high-variance region of the right-side policy, allowing the robot to deviate from the demonstrations when appropriate, as also evident in the supplementary video. Furthermore, a much smoother velocity profile can be obtained (Fig. 11).

The same policy representation can be used to encode repetitive motions as shown in Fig. 12. This fixture ($N = 1$) is learned on the $S^1 \times \mathbb{R}^2$ manifold from a demonstration of circling the launch adapter ring of the space robot setup 4 times. It is encoded in a KMP based on a GMM with $M = 5$ Gaussians with hyperparameters $\lambda = 0.1$, $\lambda_c = 10$,

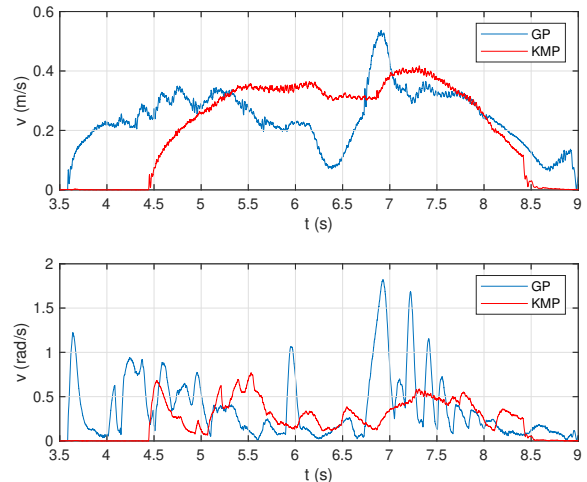


Fig. 11: Translational (upper plot) and rotational (lower plot) velocities observed during a human interaction with GP- and KMP-based velocity fixtures. Especially the rotational velocities of the KMP are much smoother than those of the GP. Furthermore, the transition from policy [1] to [2] at $t = 6.5$ s is much smoother.

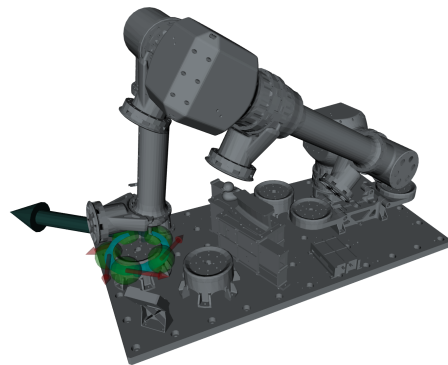


Fig. 12: Dynamical system VF on the space robot setup. The fixture contains a repeating motion in $S^1 \times \mathbb{R}^2$ around the launch lock situated just in front of the robot's end effector. This motion is overlaid with a local policy exerting a force perpendicular to the launch lock. The 5 green ellipsoids visualize the position-based covariances of the underlying GMM model with the red arrows depicting its velocities. The green arrow in the back visualizes the current output of the velocity fixture along the launch lock.

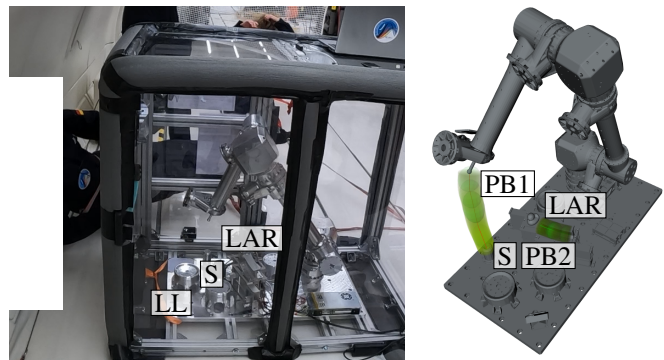


Fig. 13: Left image: The space robot setup approaching the spring [S] using an automated position-based fixture during the $0g$ phase of a parabolic flight. Also shown are the launch adapter ring segment [LAR] and the launch lock [LL]. Right image: [PB1] denotes a position-based fixture for approaching and pressing the spring assembly [S] while [PB2] shows the second position-based fixture for the robot moving along the launch adapter ring segment [LAR].

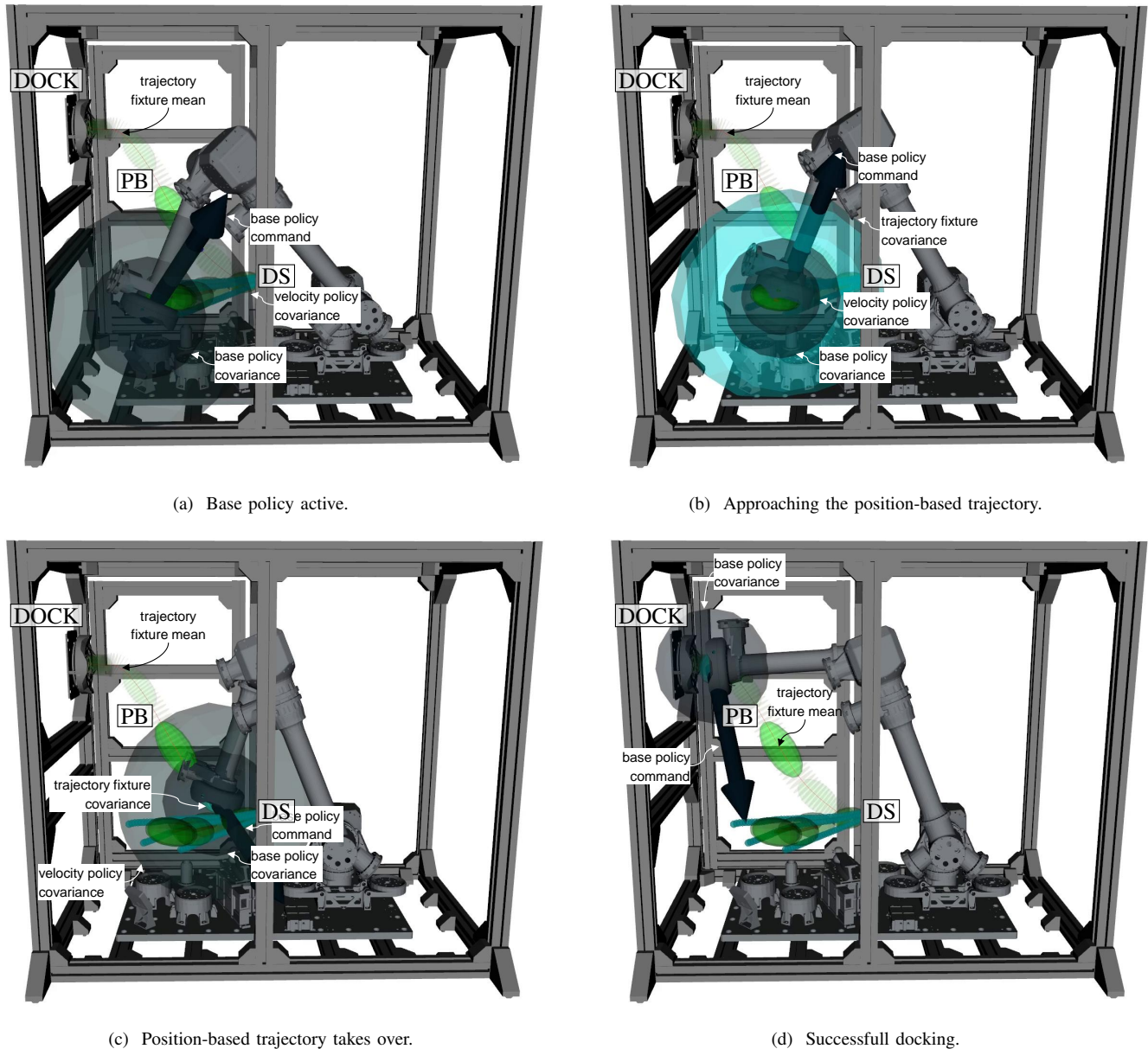


Fig. 14: Dynamical system VF $\boxed{\text{DS}}$ combined with a position-based fixture $\boxed{\text{PB}}$ on the space robot setup. The dynamical system VF guides the robot towards the start of the automated position-based fixture which performs a docking manoeuvre, where the docking interface mounted at the robot's end effector is to be docked to the interface mounted on the rack $\boxed{\text{DOCK}}$.

$\alpha = 0.1$, $h = 1$ and $l = 0.03$. The combination of learned policy and base policy pushing the robot back inside the learned region makes the robot move around the ring reliably. In addition, we make use of the probabilistic arbitration to overlay a probabilistic wrench pointing to the inside of the cylinder along the radius coordinate r with

$$\mathbf{w}_{\text{LP}} = \begin{bmatrix} 0 \\ -10N \\ 0 \end{bmatrix} \quad \Sigma_{\text{LP}} = \begin{bmatrix} 0 & 0 & 0 \\ 0 & 2 \times 10^{-4} & 0 \\ 0 & 0 & 0 \end{bmatrix}. \quad (58)$$

We evaluate the motion both on Earth as well as under $0g$ conditions on the parabolic flight with success. This shows that the velocity policy is not only suited to assist a human operator in hand-guided motion but also in fully autonomous

execution. Please see the supplementary video for details of the robot motion using our proposed DS-based formulation.

D. Automated Position-based Fixtures

For higher precision motions, where following a defined trajectory is required, an automated position-based trajectory fixture (Section VI) is well suited. We first demonstrate this fixture on the fully automated task of pressing a spring on the space robot setup with the pin end effector of the robot as visualized in Fig. 13. We learn this fixture from two kinesthetic demonstrations of pressing the spring and model the motion using $M = 5$ Gaussians. Through GMR, we retrieve a reference trajectory denoted as $\boxed{\text{PB1}}$. For the evaluation, we first move the robot to the start position of the fixture. During

the zero gravity phase of the parabolic flight, we press the spring four times with different velocities as seen in the video.

Concurrently ($N_{PB} = 2$), a second position-based fixture [PB2] is present in the robot’s workspace. However, thanks to the distance-based covariance adaptation (40), only the fixture to which the robot end effector is close to creates forces acting on the robot’s end effector. For activating this second fixture, the robot’s end effector is placed close to the [LAR]. There, the second position-based fixture learned from 4 demonstrations on the $S^1 \times \mathbb{R}^2$ manifold using $M = 5$ Gaussians gets activated. The origin of this manifold is placed at the center of the launch adapter ring radius, thus making the motion along the ring follow a perfect circle with constant radius. As in the previous section, we again overlay a probabilistic force of -10N along the radius of the cylindrical manifold, leading to the robot pressing against the [LAR]. The motion is again executed during the zero gravity phase of the parabolic flight, where the robot follows the ring while always being in contact with it guided by the perpendicular force.

E. Combining Dynamical System and Position-based Fixtures

One of the core strengths of our method is the uncertainty-aware probabilistic fusion of fixtures through (16). We therefore now evaluate the combination of VFs based on dynamical systems and position-based fixtures on the space robot setup. Figure 14 shows the scenario of docking the iBOSS “iSSI” interface mounted to the end effector of the space robot with its counterpart mounted to the rack, which we solve by combining a dynamical system VF [DS] ($N_{DS} = 1$) with a position-based trajectory fixture [PB] ($N_{PB} = 1$), both on the \mathbb{R}^3 manifold. The DS is encoded in a KMP based on a GMM with $M = 5$ Gaussians with hyperparameters $\lambda = 0.1$, $\lambda_c = 10$, $\alpha = 0.1$, $h = 1$ and $l = 0.03$. The trajectory fixture is encoded in a GMM with $M = 5$ Gaussians. As can be seen from the covariance ellipsoids of both fixtures in Fig. 14, they have similar covariance values thanks to the formulation chosen in Section V which allows for an arbitration of their wrenches even though they do not share the same representation. This allows to combine a more flexible velocity fixture with the precision coming from a position-based trajectory fixture that can model the exact approach trajectory required for a successful mating of the interface, as can be seen in the accompanying video.

F. Combining Dynamical System and Visual Servoing Fixtures

As explored in previous works [6]–[8], visual input is often required to successfully accomplish the precision requirements of a task. We therefore analyze the task of CubeSat subsystem assembly on the bilateral teleoperation setup with the aim of automating it to the extent possible. To this end, DS-based VFs allow for a flexible but relatively coarse automation. As such, they are well suited for a combination with the very precise visual servoing fixtures combined with human control.

We thus train two velocity fixtures (one for position and one for rotation guidance) resulting in $N_{DS} = 3$ on the data of [7], modelling it using a KMP with $\lambda = 0.1$, $\lambda_c = 10$, $\alpha = 0.1$ and $l = 0.03$ based on a GMM model with each $M = 5$ Gaussians.

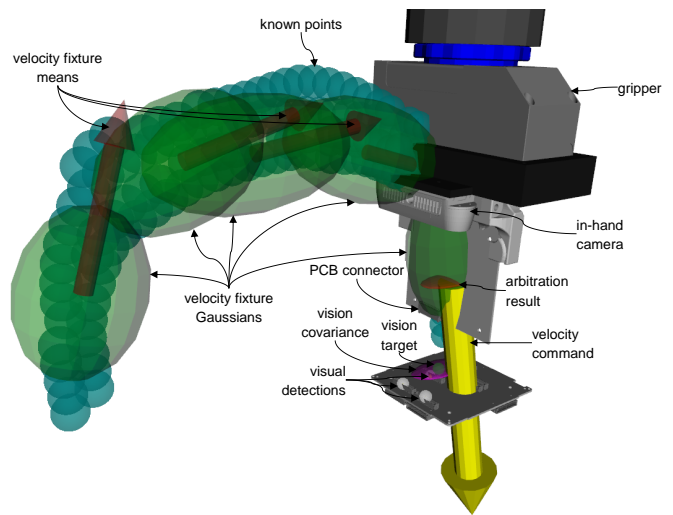


Fig. 15: Combination of DS-based and visual servoing VFs on the CubeSat subsystem assembly scenario [6]–[8]. A DS-based fixture takes the operator in the vicinity of the insertion pose where the manual visual servoing fixture takes over. This allows for a collaborative automation of the first phase of the task with no high precision requirements while the combination of the highly precise manual visual servoing fixture with human abilities allow for a successful connector insertion.

The velocity fixtures bring the subsystem to be assembled close to the assembly position where the visual servoing fixture ($N_{VS} = 1$) ensures precise alignment. Figure 15 shows the system setup, where as before two velocity fixtures, one controlling the position and the other the orientations, are combined with the visual servoing fixture taken from [8].

At the end effector pose visualized in Fig. 15, the covariance of the visual servoing fixture is, for the first time in the experiment, smaller than the covariance of the DS-based fixture. Thus, the velocity output of the latter, visualized by the yellow arrow, is not guiding the robot anymore. Instead, only the visual servoing fixture is active, reproducing the assistive behaviour introduced in [8], but combining it with the increased flexibility of the novel DS-based fixture. Notably, this enables the robot to begin from any position within its workspace, eliminating the need for initial alignment. Please see Appendix D for a description of the teleoperation coupling.

To also show the extension of the visual servoing fixture to the cylindrical manifold \mathcal{M}_2 , we set up an experiment where the task is to move test tubes from a linear holder [H1] to a cylindrical holder [H2] visualized in Fig. 16 with $N_{VS} = 2$. To simplify the implementation, we simulate visual measurements for all tube holder positions with $\Sigma = 2.25 \times 10^{-1} \cdot \mathbf{I}_6$. For the visual servoing fixture in \mathcal{M}_1 , we use the length scale $l = (0.006, 0.006, 0.2, 0, 0, 0)$ and a deadzone of 5 mm in the xy -plane. For the visual servoing fixture in \mathcal{M}_2 , we set the length scale $l = (0.1, 0.05, 0.2, 0, 0, 0)$ and use a deadzone of 0.2 rad along the angular DoF. For the DS ($N_{DS} = 3$), we again use a KMP based on a GMM with $M = 5$ Gaussians with hyperparameters $\lambda = 0.05$, $\lambda_c = 10$, $\alpha = 0.1$, $h = 1$ and $l = 0.1$ for positions respectively 0.03 for orientations. As can be seen from the supplementary video, this setup allows an operator to easily choose a test tube to pick up through guidance from a visual servoing fixture, transport it to the

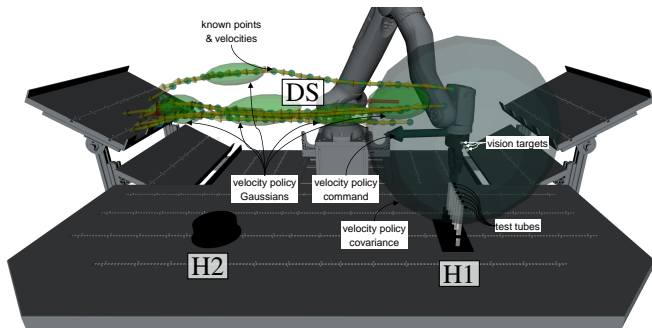


Fig. 16: Combination of dynamical system and visual servoing fixtures on the scenario of transporting test tubes from a linear holder [H1] on the right side to a circular holder [H2] on the left side. The operator is supported by a visual servoing fixture at each holder as well as a dynamical system [DS] supporting with the transportation between both holders.

other holder while the velocity fixture supports with a velocity field and by keeping the tube upright where the other visual servoing fixture eases the placement.

G. Semi-Automated Combination of All Fixtures

Finally, we combine position-based, velocity and visual servoing fixtures in one scenario ($N_{PB} = 1$, $N_{DS} = 3$, $N_{VS} = 1$; Fig. 17). The task is to pick up a bottle [B] and place it in the crate [C] supported by a position-based trajectory fixture for picking up the bottle, a velocity fixture for transporting it towards the crate and a visual servoing fixture allowing to select from multiple placement locations.

We demonstrate picking up the bottle with 3 demonstrations approaching it from different angles and learn a trajectory fixture supported by a GMM consisting of $M = 2$ Gaussians on the cylindrical manifold \mathcal{M}_2 with its coordinate system centered in the bottle. Due to its high covariance along the angle ϕ of the manifold, the variable stiffness formulation sets a very low stiffness for this DoF, allowing the bottle to be picked up from multiple angles (Fig. 17). As in Section VIII-B, using the covariance-aware attractor point calculation from (38) and (39) is again crucial. Through this formulation, the robot end effector can be moved in the plane while always pointing the gripper towards the bottle. The precision matrix at the robot configuration of Fig. 17 evaluates to

$$P = \begin{bmatrix} 10 & 11 & 8 & -11 & 17 & 31 \\ 11 & 762 & -18 & 79 & 9 & 54 \\ 8 & -18 & 990 & -7 & 27 & 1 \\ -11 & 79 & -7 & 738 & 97 & -11 \\ 17 & 9 & 27 & 97 & 312 & 42 \\ 31 & 54 & 1 & -11 & 42 & 822 \end{bmatrix}. \quad (59)$$

With $\lambda_{rot}^- = 100$, $\lambda_{rot}^+ = 500$, $\lambda_{trans}^- = 100$, $\lambda_{trans}^+ = 500$, $k_{trans,nom} = 500$ and $k_{rot,nom} = 40$, we obtain the stiffness

$$K = \begin{bmatrix} * & 3.6 & 8.2 & 5.4 & 5.5 & 2.8 \\ 7.3 & 490 & -2.1 & 49 & 4.5 & 35 \\ 4.1 & * & 490 & -2.7 & 13 & 1.2 \\ * & 50 & -2.6 & 43 & 6.5 & 3.7 \\ * & -23 & 9.6 & 1.8 & 12 & -2.6 \\ * & 35 & 1.3 & 3.8 & * & 41 \end{bmatrix} \quad (60)$$

with * denoting values < 1 . Another crucial component is the covariance adaptation using the Mahalanobis distance

(Section VI-C). Setting a maximum distance value of 5 for the unitless Mahalanobis distance, the fixture remains active for larger displacements around the rotational DoF (up to 41°) than for the other DoFs (up to 7.1 cm) for the given precision. Once the bottle has been picked up, the operator can easily escape this fixture by achieving a displacement larger than this threshold to deactivate the position-based fixture.

After leaving the position-based VF, the DS-based VF takes over. This DS learned from 5 demonstrations is encoded in a KMP based on a GMM with $M = 5$ Gaussians with hyperparameters $\lambda = 0.1$, $\lambda_c = 10$, $\alpha = 0.1$, $h = 1$ and $l = 0.1$ for the position velocity and $l = 0.03$ for the orientation velocity field. This DS moves the operator towards the visual servoing VF while keeping the bottle upright.

We again simulate visual measurements for all $M = 20$ crate positions with $\Sigma = 2.25 \times 10^{-1} \cdot \mathbf{I}_6$. For the visual servoing fixture, we use a length scale $l = (0.006, 0.006, 0.2, 0, 0, 0)$ and a deadzone of 5 mm in the xy plane.

The supplementary video shows how the combination of VFs based on different representations ensures required guidance through the task with smooth transitions.

IX. DISCUSSION

A. Dynamical-Systems-based Virtual Fixtures

VFs based on DSs as evaluated also in combination with other fixtures in Sections VIII-C and VIII-E to VIII-G allow for a collaborative automation. By default, the task is being performed autonomously while human interaction is always possible as can be seen in the supplementary video.

A major challenging problem in DS-based VFs is the need to find the right hyperparameters both for modeling the learned policy as well as for the base policy. When using a GP for modeling the DS, it is especially important to choose the covariance while ensuring its covariance output fits the other fixtures in the workspace, i.e. it should not output a too low covariance when another, better suited fixture should take over. On the other hand, its uncertainty should also not be too high as it would not take any effect otherwise. This modelling is greatly simplified through the use of KMP-based policies, where the underlying GMM already models the covariance appropriately. This leaves the covariance tuning to the base policy, which is equipped with a constant covariance through (35). Future work should consider approaches to automatically select viable hyperparameters in the fixture's kernel as well as for this constant covariance value from demonstrations.

A limitation of the current formulation is that only a global, but no per-DoF epistemic uncertainty estimate of the velocity policy is available through the kernels (31). This was alleviated in the the evaluation through the usage of different policies for positional and orientational control; however, as for the coupled stiffness (Section IV-B), a policy unifying all DoFs would be desirable. Such policy could then, through the arbitration (16), progress some DoFs through the DS evolution while the remaining DoFs would be brought back to the demonstration data thanks to the base policy. Such behaviour is especially relevant in shared control, where perturbations induced by the operator are a desired property of the overall system.

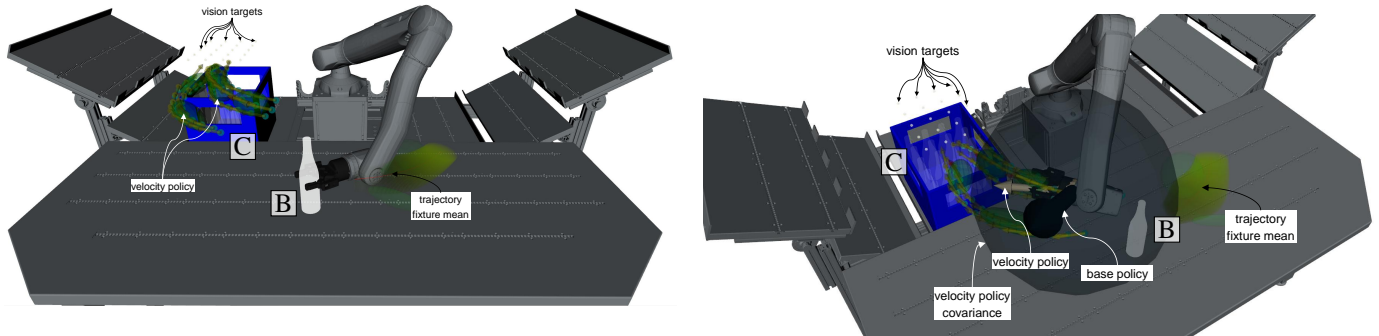


Fig. 17: Picking up a bottle [B] for moving it into a crate [C] using position-based trajectory, velocity and visual servoing fixtures. As visualized on the left, the rotationally symmetric bottle can be picked up from any angle thanks to a probabilistic trajectory fixture learned from demonstrations on \mathcal{M}_2 with variable stiffness leading to the stiffness matrix in (60). After [B] has been picked up, the velocity fixture takes over, fusing a base policy with the learned policy (right side). This fixture aids the operator to move to [C] where a probabilistic visual servoing fixture allows to select different placement positions.

B. Probabilistic Policy Arbitration via Products of Experts

Previous works have already shown that a probabilistic arbitration scheme allows for an optimal combination of different VFs [8]. Throughout the evaluation, we have seen how this arbitration naturally extends to other types of VFs and how different geometries can be incorporated. This allows to always choose the best VF representation for a specific task phase without manually designing transitions, highlighting the advantages of our fully probabilistic VF formulation. One key distinction to previous works is that our formulation supports different manifolds \mathcal{M} by transforming the wrench to a common representation in the cotangent space of $\mathbb{R}^3 \times \mathcal{S}^3$. By fusing the different fixtures in wrench space, naturally, different types of VFs are supported. This allows to easily fuse fixtures calculating an attractor point, a target velocity or directly a wrench in a unified formulation which in turn allows to model guiding behaviour for each portion of a task using the best available fixture representation.

C. Variable Stiffness

Previous works [8], [44] either considered diagonal or block-diagonal stiffness matrices. While such formulations are well suited for scenarios where high covariance only appears within positions or orientations, block-diagonal stiffness matrices fail with the experiment described in Section VIII-A as this requires to respect a lower stiffness along a coupled DoF. Clearly, such coupled variable stiffness is only possible with our method. In this experiment, our approach achieves to model a stiffness that makes the robot’s end effector follow the geodesic between two detections. Our approach furthermore provides reasonable stiffness values for the precision matrices observed in all experiments. This underlines that the proposed approach is suitable for the generation of stiffness matrices from arbitrary precision matrices.

X. CONCLUSION

In this work we introduced a unified, probabilistic Virtual Fixture framework that provides different types of assistance to operators – particularly **coarse**, **precise** and **very precise**

guidance – where each type of fixture can be either manually defined or learned from human demonstrations. To address a gap in the literature – namely, the limited attention given to learned virtual fixtures that actively support task progression – we propose a novel, uncertainty-aware Dynamical System-based Virtual Fixture formulation that enables flexible task automation while keeping the operator in control. We further introduce geometry-awareness in shared control through object-specific coordinate systems, including Cartesian, cylindrical and spherical frames. Combined with a novel variable impedance formulation – which robustly captures demonstrated correlations between DoFs – our framework brings together the different fixture types using a *product of experts* approach, enabling a principled and uncertainty-aware fusion of assistance commands.

We have shown experimentally that the approach can be readily applied across diverse use cases, thanks to its ease of programming and flexibility with respect to fixture representations, input modalities, and uncertainty sources. While we demonstrated its use in factory automation and space scenarios, we believe the approach is also well-suited for medical and personal assistance robotics, which we plan to investigate in future work. We furthermore envision developing methods to interactively modify position-based fixtures, allowing an operator to modify them adaptively based on novel task needs [64]. Finally, to enable the use of the proposed framework in high-latency applications such as on-orbit servicing, we plan to integrate it with controllers that can provide stable force feedback despite such delays.

REFERENCES

- [1] L. Rosenberg, “Virtual fixtures: Perceptual tools for telerobotic manipulation,” in *Proceedings of IEEE Virtual Reality Annual International Symposium*, 1993, pp. 76–82.
- [2] S. A. Bowyer, B. L. Davies, and F. R. y Baena, “Active constraints/virtual fixtures: A survey,” *IEEE Transactions on Robotics*, vol. 30, no. 1, pp. 138–157, Feb 2014.
- [3] K. Haggmann, A. Hellings-Kuss, F. Steidle, F. Stulp, D. Leidner, and J. Klodmann, “Continuous transitions between levels of autonomy based on virtual fixtures for surgical robotic systems,” in *2024 IEEE/RSJ International Conference on Intelligent Robots and Systems, IROS 2024 (submitted)*, 2024. [Online]. Available: <https://elib.dlr.de/203851/>

- [4] A. Wicht, T. Franke, A. Hahn, N. Håkansson, C. Kürbis, R. Smol, T. Hulin, T. Eiband, P. Lehner, M. Mühlbauer, K. Nottensteiner, R. Pietschmann, B. Thaler, D. Thaler, and J. Bosse, "Human-centric concept for a reconfigurable robotic system enabling low-volume assembly of photonic and quantum modules," in *2025 IEEE/SICE International Symposium on System Integration (SII)*. IEEE, pp. 1241–1246.
- [5] F. Leutert, D. Bohlig, F. Kempf, K. Schilling, M. Mühlbauer, B. Ayan, T. Hulin, F. Stulp, A. Albu-Schäffer, V. Kutscher, C. Plesker, T. Dasbach, S. Damm, R. Anderl, and B. Schleich, "Ai-enabled cyber-physical in-orbit factory - ai approaches based on digital twin technology for robotic small satellite production," vol. 217, pp. 1–17.
- [6] M. S. Mühlbauer, F. Leutert, C. Plesker, L. X. Wiedmann, A. M. Giordano, J. Silverio, T. Hulin, F. Stulp, J. Voges, R. Knobloch, K. Schilling, B. Schleich, and A. O. Albu-Schäffer, "Ai-based robust and failure-tolerant processes for in-orbit manufacturing of modular small satellites," in *75th International Astronautical Congress, IAC 2024*, October 2024. [Online]. Available: <https://elib.dlr.de/206962/>
- [7] M. Mühlbauer, F. Steinmetz, F. Stulp, T. Hulin, and A. Albu-Schäffer, "Multi-phase multi-modal haptic teleoperation," in *2022 IEEE/RSJ International Conference on Intelligent Robots and Systems (IROS)*. IEEE.
- [8] M. Mühlbauer, T. Hulin, B. Weber, S. Calinon, F. Stulp, A. Albu-Schäffer, and J. Silvério, "A probabilistic approach to multi-modal adaptive virtual fixtures," *IEEE Robotics and Automation Letters*, vol. 9, no. 6, pp. 5298–5305, 2024.
- [9] A. Birk, G. Antonelli, P. Di Lillo, E. Simetti, G. Casalino, G. Indiveri, L. Ostuni, A. Turetta, A. Caffaz, P. Weiss, T. Gobert, T. Doernbach, B. Chemisky, J. Gancet, T. Siedel, S. Govindaraj, X. Martinez, P. Letier, C. Mueller, T. Luczynski, A. Gomez Chavez, D. Koehntopp, A. Kupcsik, S. Calinon, and A. K. Tanwani, "Dexterous underwater manipulation from onshore locations: Streamlining efficiencies for remotely operated underwater vehicles," vol. 25, no. 4, pp. 24–33.
- [10] A. Ijspeert, J. Nakanishi, and S. Schaal, "Movement imitation with nonlinear dynamical systems in humanoid robots," in *2002 IEEE International Conference on Robotics and Automation*. IEEE, pp. 1398–1403.
- [11] A. J. Ijspeert, J. Nakanishi, H. Hoffmann, P. Pastor, and S. Schaal, "Dynamical movement primitives: Learning attractor models for motor behaviors," *Neural Computation*, vol. 25, no. 2, pp. 328–373, 2013.
- [12] M. Saveriano, F. J. Abu-Dakka, A. Kramberger, and L. Peternel, "Dynamic movement primitives in robotics: A tutorial survey," *The International Journal of Robotics Research*, vol. 42, no. 13, pp. 1133–1184, 2023.
- [13] P. C. Lopez-Custodio, K. Bharath, A. Kucukyilmaz, and S. Preston, "Non-parametric regression for robot learning on manifolds," *arXiv preprint arXiv:2310.19561*, 2023.
- [14] B. Fichera, S. Borovitskiy, A. Krause, and A. G. Billard, "Implicit manifold gaussian process regression," in *Advances in Neural Information Processing Systems*, A. Oh, T. Naumann, A. Globerson, K. Saenko, M. Hardt, and S. Levine, Eds., vol. 36. Curran Associates, Inc., 2023, pp. 67 701–67 720.
- [15] S. M. Khansari-Zadeh and A. Billard, "Learning stable nonlinear dynamical systems with gaussian mixture models," *IEEE Transactions on Robotics*, vol. 27, no. 5, pp. 943–957, 2011.
- [16] B. Fichera and A. Billard, "Linearization and identification of multiple-attractor dynamical systems through laplacian eigenmaps," *J. Mach. Learn. Res.*, vol. 23, no. 1, Jan 2022.
- [17] —, "Learning dynamical systems encoding non-linearity within space curvature," 2024. [Online]. Available: <https://arxiv.org/abs/2403.11948>
- [18] H. B. Mohammadi, S. Hauberg, G. Arvanitidis, N. Figueroa, G. Neumann, and L. Rozo, "Neural contractive dynamical systems," in *The Twelfth International Conference on Learning Representations*, 2023.
- [19] R. Pérez-Dattari, C. Della Santina, and J. Kober, "Puma: Deep metric imitation learning for stable motion primitives," *Advanced Intelligent Systems*, vol. 6, no. 11, 2024.
- [20] R. Pérez-Dattari and J. Kober, "Stable motion primitives via imitation and contrastive learning," *IEEE Transactions on Robotics*, vol. 39, no. 5, pp. 3909–3928, 2023.
- [21] G. Raiola, S. S. Restrepo, P. Chevalier, P. Rodriguez-Ayerbe, X. Lamy, S. Tliha, and F. Stulp, "Co-manipulation with a library of virtual guiding fixtures," *Autonomous Robots*, vol. 42, no. 5, pp. 1037–1051, Nov 2017.
- [22] B. Ti, A. Razmjoo, Y. Gao, J. Zhao, and S. Calinon, "A geometric optimal control approach for imitation and generalization of manipulation skills," *Robotics and Autonomous Systems*, vol. 164, p. 104413, 2023.
- [23] G. Franzese, A. Meszaros, L. Peternel, and J. Kober, "Ilosa: Interactive learning of stiffness and attractors," in *2021 IEEE/RSJ International Conference on Intelligent Robots and Systems (IROS)*. IEEE, pp. 7778–7785.
- [24] A. Meszaros, G. Franzese, and J. Kober, "Learning to pick at non-zero-velocity from interactive demonstrations," *IEEE Robotics and Automation Letters*, vol. 7, no. 3, pp. 6052–6059, 2022.
- [25] E. Pignat and S. Calinon, "Bayesian gaussian mixture model for robotic policy imitation," *IEEE Robotics and Automation Letters*, vol. 4, no. 4, pp. 4452–4458, 2019.
- [26] D. Papageorgiou, F. Dimeas, T. Kastritsi, and Z. Doulgeri, "Kinesthetic guidance utilizing dmp synchronization and assistive virtual fixtures for progressive automation," *Robotica*, vol. 38, no. 10, pp. 1824–1841, 2019.
- [27] A. Pervez, H. Latifee, J.-H. Ryu, and D. Lee, "Motion encoding with asynchronous trajectories of repetitive teleoperation tasks and its extension to human-agent shared teleoperation," *Autonomous Robots*, vol. 43, no. 8, pp. 2055–2069, 2019.
- [28] X. Chen, Y. Michel, and D. Lee, "Closed-loop variable stiffness control of dynamical systems," in *2020 IEEE-RAS 20th International Conference on Humanoid Robots (Humanoids)*. IEEE.
- [29] H. Xue, Y. Michel, and D. Lee, "A shared control approach based on first-order dynamical systems and closed-loop variable stiffness control," *Journal of Intelligent & Robotic Systems*, vol. 109, no. 4, 2023.
- [30] W. Amanhoud, M. Khoramshahi, and A. Billard, "A dynamical system approach to motion and force generation in contact tasks," in *Proceedings of Robotics: Science and Systems*, June 2019.
- [31] K. Hagmann, A. Hellings-Kuß, J. Klodmann, R. Richter, F. Stulp, and D. Leidner, "A digital twin approach for contextual assistance for surgeons during surgical robotics training," *Frontiers in Robotics and AI*, vol. 8, 2021.
- [32] V. Pruks and J.-H. Ryu, "Method for generating real-time interactive virtual fixture for shared teleoperation in unknown environments," *The International Journal of Robotics Research*, vol. 41, no. 9–10, pp. 925–951, 2022.
- [33] A. Bettini, P. Marayong, S. Lang, A. Okamura, and G. Hager, "Vision-assisted control for manipulation using virtual fixtures," *IEEE Transactions on Robotics*, vol. 20, no. 6, pp. 953–966, 2004.
- [34] M. J. A. Zeestraten, I. Havoutis, and S. Calinon, "Programming by demonstration for shared control with an application in teleoperation," *IEEE Robotics and Automation Letters*, vol. 3, no. 3, pp. 1848–1855, 2018.
- [35] J. J. Abbott, P. Marayong, and A. M. Okamura, "Haptic virtual fixtures for robot-assisted manipulation," in *Robotics Research: Results of the 12th International Symposium ISRR*. Springer, 2007, pp. 49–64.
- [36] Z. Pezzementi, A. M. Okamura, and G. D. Hager, "Dynamic guidance with pseudoadmittance virtual fixtures," in *Proceedings 2007 IEEE International Conference on Robotics and Automation*, 2007, pp. 1761–1767.
- [37] M. Selvaggio, M. Cognetti, S. Nikolaidis, S. Ivaldi, and B. Siciliano, "Autonomy in physical human-robot interaction: A brief survey," *IEEE Robotics and Automation Letters*, vol. 6, no. 4, pp. 7989–7996, 2021.
- [38] M. Selvaggio, G. Notomista, F. Chen, B. Gao, F. Trapani, and D. Caldwell, "Enhancing bilateral teleoperation using camera-based online virtual fixtures generation," in *2016 IEEE/RSJ International Conference on Intelligent Robots and Systems (IROS)*. IEEE.
- [39] F. Abi-Farraj, C. Pacchierotti, O. Arenz, G. Neumann, and P. R. Giordano, "A haptic shared-control architecture for guided multi-target robotic grasping," *IEEE Transactions on Haptics*, vol. 13, no. 2, pp. 270–285, 2020.
- [40] Y. Michel, R. Rahal, C. Pacchierotti, P. R. Giordano, and D. Lee, "Bilateral teleoperation with adaptive impedance control for contact tasks," *IEEE Robotics and Automation Letters*, vol. 6, no. 3, pp. 5429–5436, 2021.
- [41] N. Hogan, "Impedance control: An approach to manipulation," in *1984 American Control Conference*. IEEE.
- [42] Y. Michel, M. Saveriano, F. J. Abu-Dakka, and D. Lee, "Orientation control with variable stiffness dynamical systems," in *2023 IEEE/RSJ International Conference on Intelligent Robots and Systems (IROS)*. IEEE.
- [43] R. Balachandran, M. De Stefano, H. Mishra, C. Ott, and A. Albu-Schaeffer, "Passive arbitration in adaptive shared control of robots with variable force and stiffness scaling," *Mechatronics*, vol. 90, p. 102930, 2023.
- [44] F. Abi-Farraj, T. Osa, N. P. J. Peters, G. Neumann, and P. R. Giordano, "A learning-based shared control architecture for interactive task execution," in *2017 IEEE International Conference on Robotics and Automation (ICRA)*. IEEE.
- [45] S. Huang and J. M. Schimmels, "Achieving an Arbitrary Spatial Stiffness with Springs Connected in Parallel," *Journal of Mechanical Design*, vol. 120, no. 4, pp. 520–526, 12 1998.

- [46] S. Huang and J. Schimmels, “The eigenscrew decomposition of spatial stiffness matrices,” *IEEE Transactions on Robotics and Automation*, vol. 16, no. 2, pp. 146–156, 2000.
- [47] M. J. A. Zeestraten, I. Havoutis, J. Silvério, S. Calinon, and D. G. Caldwell, “An approach for imitation learning on Riemannian manifolds,” *IEEE Robotics and Automation Letters*, vol. 2, no. 3, pp. 1240–1247, 2017.
- [48] S. Calinon, “Gaussians on riemannian manifolds: Applications for robot learning and adaptive control,” *IEEE Robotics & Automation Magazine*, vol. 27, no. 2, pp. 33–45, 2020.
- [49] J. M. Lee, *Introduction to Smooth Manifolds*. Springer New York.
- [50] S. Calinon, “A tutorial on task-parameterized movement learning and retrieval,” *Intelligent Service Robotics*, vol. 9, no. 1, pp. 1–29, Sep 2015.
- [51] R. A. Jacobs, M. I. Jordan, S. J. Nowlan, and G. E. Hinton, “Adaptive mixtures of local experts,” *Neural Computation*, vol. 3, no. 1, pp. 79–87, 1991.
- [52] C. K. Williams and C. E. Rasmussen, *Gaussian processes for machine learning*. MIT press Cambridge, MA, 2006, vol. 2, no. 3.
- [53] Y. Huang, L. Rozo, J. Silvério, and D. G. Caldwell, “Kernelized movement primitives,” *The International Journal of Robotics Research*, vol. 38, no. 7, pp. 833–852, 2019.
- [54] N. Jaquier, V. Borovitskiy, A. Smolensky, A. Terenin, T. Asfour, and L. Rozo, “Geometry-aware bayesian optimization in robotics using riemannian matérn kernels,” in *Proceedings of the 5th Conference on Robot Learning*, ser. Proceedings of Machine Learning Research, A. Faust, D. Hsu, and G. Neumann, Eds., vol. 164. PMLR, 08–11 Nov 2022, pp. 794–805.
- [55] G. Hinton, “Products of experts,” in *9th International Conference on Artificial Neural Networks: ICANN ’99*, vol. 1999. IEEE, pp. 1–6.
- [56] M. Dyck, A. Sachtler, J. Klodmann, and A. Albu-Schaffer, “Impedance control on arbitrary surfaces for ultrasound scanning using discrete differential geometry,” *IEEE Robotics and Automation Letters*, vol. 7, no. 3, pp. 7738–7746, 2022.
- [57] G. Chen, H. Wang, Z. Lin, and X. Lai, “The principal axes decomposition of spatial stiffness matrices,” *IEEE Transactions on Robotics*, vol. 31, no. 1, pp. 191–207, 2015.
- [58] S. Huang and J. M. Schimmels, “Comments on “the principal axes decomposition of spatial stiffness matrices”,” *IEEE Transactions on Robotics*, vol. 31, no. 6, pp. 1561–1564, 2015.
- [59] S. Calinon and D. Lee, “Learning control,” in *Humanoid robotics: A reference*. Springer Netherlands, 2017, pp. 1–52.
- [60] M. Hutchinson, A. Terenin, V. Borovitskiy, S. Takao, Y. Teh, and M. Deisenroth, “Vector-valued gaussian processes on riemannian manifolds via gauge independent projected kernels,” in *Advances in Neural Information Processing Systems*, M. Ranzato, A. Beygelzimer, Y. Dauphin, P. Liang, and J. W. Vaughan, Eds., vol. 34, 2021, pp. 17 160–17 169.
- [61] S. Salvador and P. Chan, “Toward accurate dynamic time warping in linear time and space,” *Intelligent Data Analysis*, vol. 11, no. 5, pp. 561–580, 2007.
- [62] C. M. Bishop, *Pattern Recognition and Machine Learning (Information Science and Statistics)*. Springer, 2006.
- [63] M. S. Mühlbauer, F. Stulp, A. O. Albu-Schäffer, and J. Silvério, “Mixture of experts on riemannian manifolds for visual-servoing fixtures,” in *2022 IEEE/RSJ International Conference on Intelligent Robots and Systems, Workshop on Probabilistic Robotics in the Age of Deep Learning*, Oktober 2022. [Online]. Available: <https://elib.dlr.de/189970/>
- [64] G. Quere, F. Stulp, D. Filliat, and J. Silvério, “A probabilistic approach for learning and adapting shared control skills with the human in the loop,” in *2024 IEEE International Conference on Robotics and Automation (ICRA)*. IEEE, pp. 15 728–15 734.
- [65] A. Albu-Schäffer, C. Ott, U. Frese, and G. Hirzinger, “Cartesian impedance control of redundant robots: recent results with the dlr-light-weight-arms,” in *2003 IEEE International Conference on Robotics and Automation (Cat. No.03CH37422)*, vol. 3, 2003, pp. 3704–3709 vol.3.

APPENDIX

A. Key Notations

Table II summarizes the key notations of our framework.

B. Variable Impedance Control on Cylindrical and Spherical Manifolds

The variable impedance formulation of Section IV-B can also be extended to cylindrical and spherical manifolds in-

TABLE II: KEY NOTATIONS USED IN OUR FRAMEWORK.

$N \in \mathbb{N}$	\triangleq	Number of data points per demonstration
N_{DS}, N_{PB}, N_{VS}	\triangleq	Number of fixtures of each type
M	\triangleq	Number of Gaussian components in a fixture
$\mathbf{x}_{VF,i}$	\triangleq	Attractor of the i -th fixture
$\mathbf{w}_{VF,i}$	\triangleq	Wrench of the i -th fixture
$\Sigma_{VF,i}$	\triangleq	Covariance of the i -th fixture
$\mathbf{K}_{VF,i}$	\triangleq	Stiffness matrix of the i -th fixture
$\mathbf{D}_{VF,i}$	\triangleq	Damping matrix of the i -th fixture
\mathbf{k}_{nom}	\triangleq	Diagonal nominal stiffness values
$\lambda_{trans}^-, \lambda_{trans}^+$	\triangleq	“High” and “low” translational stiffness eigenvalues
$\lambda_{rot}^-, \lambda_{rot}^+$	\triangleq	“High” and “low” rotational stiffness eigenvalues
$\lambda, \lambda_c, \alpha$	\triangleq	Regularization and scaling factors of the KMP
l	\triangleq	Length scale for the RBF kernel
\mathbf{L}	\triangleq	Length scale of the visual servoing fixture
γ	\triangleq	Regularization factor
\mathbf{L}_{dead}	\triangleq	Length scale of the deadzone

roduced in Section III-A. For this, we scale the nominal translational stiffness $k_{nom,j}$ by the radius r for the angular DoFs ($\mathcal{M}_2: j = 1, \mathcal{M}_3: j = 1, 2$), i.e.

$$k_{nom,j}^* = r \cdot k_{nom,j}. \quad (61)$$

This ensures a stiffness comparable to the Euclidean case for those DoFs, avoiding too high stiffness values for $r \ll 1$. As the calculation of the stiffness values is performed in a coordinate system rotated by \mathbf{R}_{diag}^\top , the maximum translational stiffness values for each DoF in those coordinates has to be limited further s.t. when rotating the stiffness matrix back, the nominal stiffness value is not exceeded. This can be achieved by limiting the maximum value of the stiffness $\mathbf{k}_{nom,trans}$ denoting the translational ($j = 1, 2, 3$) DoFs of \mathbf{k}_{nom} in rotated DoFs through

$$\mathbf{k}_{rot} = \text{diag}(\mathbf{R}_{diag}^\top \text{diag}(\mathbf{k}_{nom,trans}) \mathbf{R}_{diag}) \quad (62)$$

$$\mathbf{k}_{rotback} = \text{diag}(\mathbf{R}_{diag} \text{diag}(\mathbf{k}_{rot}) \mathbf{R}_{diag}^\top) \quad (63)$$

$$\beta = \max(\mathbf{k}_{rotback} \oslash \mathbf{k}_{nom,trans}) \quad (64)$$

$$\mathbf{k}'_{nom,trans} = \beta \mathbf{k}_{rot} \quad (65)$$

where diag transforms a vector to a diagonal matrix respectively extracts the diagonal of a matrix and \oslash is the elementwise vector division. In (62), we take the diagonal elements of $\mathbf{k}_{nom,trans}$ rotated into coordinates of $\mathbf{P}'_{VF,i}$. As the maximum values of the translational stiffnesses correspond to $\text{diag}(\mathbf{k}_{rot})$, we can rotate that matrix back and check for potentially increased stiffness values in (64). The maximum value of this increase is then used to scale the translational stiffnesses.

C. Optimal Damping using Double Diagonalization

To achieve an optimal damping for \mathbf{K}_i from Section IV-B, we design the damping matrix \mathbf{D}_i using the factorization approach presented in [65] with $\zeta = 0.7$, in particular

$$\mathbf{D}_i = \zeta (\mathbf{M}_{i,1} \mathbf{K}_{i,1}^* + \mathbf{K}_{i,1}^* \mathbf{M}_{i,1}) \quad (66)$$

with the stiffness matrix $\mathbf{K}_i^* = \mathbf{K}_{i,1}^* \mathbf{K}_{i,1}^*$ and the mass matrix $\mathbf{M}_{i,\mathcal{M}} = \mathbf{M}_{i,1} \mathbf{M}_{i,1}$. Similar to the wrench transformation in

the previous section, a Cartesian stiffness matrix \mathbf{M}_{cart} at the end effector has to be transformed to the manifold using

$$\mathbf{M}_{i,\mathcal{M}} = (\mathbf{J}_{i,\mathcal{M}} \mathbf{M}_{\text{cart}}^{-1} \mathbf{J}_{i,\mathcal{M}}^\top)^{-1}. \quad (67)$$

To also achieve damping along DoFs with no stiffness, we calculate \mathbf{K}_i^* with scaling factors s_j used in (21) and (23) lower-bounded to a small value $\epsilon > 0$. This small damping ensures smoothly decaying robot motions.

D. Teleoperation System

To supply the operator with force feedback, we use the bilateral teleoperation system of [7], [8]. We assume that the haptic input device can also be controlled using Cartesian wrenches; in case of a torque-controlled robot, (3) can be used to compute joint torques. Using a simple position-computed force architecture that does not require a force-torque sensor at the end effector, the Cartesian wrenches of remote robot $\mathbf{w}_{\text{ee,rem}}$ and input device $\mathbf{w}_{\text{ee,inp}}$ are

$$\mathbf{w}_{\text{ee,rem}} = \chi \left(\mathbf{K} \text{Log}_{\mathbf{x}_{\text{ee}}}^{\mathcal{M}}(\mathbf{x}_{\text{inp}}) + \mathbf{D} \frac{d}{dt} \text{Log}_{\mathbf{x}_{\text{ee}}}^{\mathcal{M}}(\mathbf{x}_{\text{inp}}) \right) + \mathbf{w}_{\text{VF}} \quad (68)$$

$$\mathbf{w}_{\text{ee,inp}} = -\chi \mathbf{A} \mathbf{d}_{\text{ir}} \mathbf{w}_{\text{ee,remote}}. \quad (69)$$

The user receives force feedback from both the environment as well as the VFs through the coupling introduced by χ , the adjoint $\mathbf{A} \mathbf{d}_{\text{ir}}$ transforms wrenches between coordinate systems of the remote robot and the input device. By applying the VF wrench to the robot performing the task, we can support a user while avoiding potential inaccuracies resulting from a teleoperated coupling.

E. Coordinate System Conversions

1) *Conversion between $\mathcal{S}^1 \times \mathbb{R}^2 \times \mathcal{S}^3$ and $\mathbb{R}^3 \times \mathcal{S}^3$* : Position quantities can be converted from \mathcal{M}_1 to \mathcal{M}_2 using

$$\theta_c = x/r, \quad \theta_s = y/r, \quad r = \sqrt{x^2 + y^2}, \quad z = z \quad (70)$$

where θ_c and θ_s denote the angle θ around the z axis as complex number. For small r , the angle θ is not well-defined. The quaternion has to be rotated by $-\theta$, specifically

$$\mathbf{q}^{\mathcal{M}_2} = \text{Exp}_{\mathbf{I}}^{\mathcal{S}^3} \begin{bmatrix} 0 \\ 0 \\ -\theta \end{bmatrix} \cdot \mathbf{q}^{\mathcal{M}_1}. \quad (71)$$

The inverse conversion can be performed as follows

$$x = r \cdot \theta_c, \quad y = r \cdot \theta_s, \quad z = z, \quad \mathbf{q}^{\mathcal{M}_1} = \text{Exp}_{\mathbf{I}}^{\mathcal{S}^3} \begin{bmatrix} 0 \\ 0 \\ \theta \end{bmatrix} \cdot \mathbf{q}^{\mathcal{M}_2} \quad (72)$$

with $\theta = \arctan2(\theta_s, \theta_c)$ where $\arctan2$ is the modified arcus tangens mapping to the full circle $[-\pi, \pi]$.

2) *Conversion between $\mathcal{S}^2 \times \mathbb{R}^1 \times \mathcal{S}^3$ and $\mathbb{R}^3 \times \mathcal{S}^3$* : Position quantities can be converted from \mathcal{M}_1 to \mathcal{M}_3 using

$$s_0 = x/r, \quad s_1 = y/r, \quad s_2 = z/r, \quad r = \sqrt{x^2 + y^2 + z^2} \quad (73)$$

Note that for very small r , the values s_i are not well-defined. The quaternion expressing the orientation has to be rotated by the inverse of the rotation $\mathbf{q}_{\text{align}}$ aligning $[0, 0, 1]$ with $[s_0, s_1, s_2]$, specifically

$$\mathbf{q}^{\mathcal{M}_3} = \mathbf{q}_{\text{align}}^{-1} \cdot \mathbf{q}^{\mathcal{M}_1}. \quad (74)$$

The inverse conversion can be performed as follows

$$x = r \cdot s_0, \quad y = r \cdot s_1, \quad z = r \cdot s_2, \quad \mathbf{q}^{\mathcal{M}_1} = \mathbf{q}_{\text{align}} \cdot \mathbf{q}^{\mathcal{M}_3}. \quad (75)$$

F. Manifold Jacobians

The manifold Jacobian $\mathbf{J}_{\mathcal{M}} = \frac{\partial \mathbf{x}_{\text{ee},i,\mathcal{M}}}{\partial \mathbf{x}_{\text{ee},\mathbb{R}^3 \times \mathcal{S}^3}}$ relating $\dot{\mathbf{x}}^{\mathcal{M}} = \mathbf{J}_{\mathcal{M}} \dot{\mathbf{x}}^{\mathbb{R}^3 \times \mathcal{S}^3}$ and $\mathbf{w}^{\mathbb{R}^3 \times \mathcal{S}^3} = \mathbf{J}_{\mathcal{M}}^\top \mathbf{w}^{\mathcal{M}}$ is derived as in [56]

$$\mathbf{J}_{\mathcal{M}} = \begin{bmatrix} \mathbf{J}_{\mathbf{px}} & \mathbf{0} \\ \mathbf{J}_{\omega\mathbf{x}} & \mathbf{J}_{\omega\omega} \end{bmatrix} \quad (76)$$

where $\mathbf{J}_{\mathbf{px}}$ denotes position quantities and $\mathbf{J}_{\omega\mathbf{x}}$ the coupling between position and orientation. Both are given for \mathcal{M}_2 and \mathcal{M}_3 in the following. We furthermore have $\mathbf{J}_{\omega\omega} = \mathbf{I}$ for \mathcal{M} as the axes of the orientation always coincide.

1) *$\mathcal{S}^1 \times \mathbb{R}^2 \times \mathcal{S}^3$ Jacobian*: Both Cartesian x and y coordinates have an influence on the angular DoF of the manifold and on r , specifically

$$\mathbf{J}_{\mathbf{px}} = \begin{bmatrix} \frac{-y}{x^2+y^2} & \frac{x}{x^2+y^2} & 0 \\ \frac{x}{\sqrt{x^2+y^2}} & \frac{y}{\sqrt{x^2+y^2}} & 0 \\ 0 & 0 & 1 \end{bmatrix}. \quad (77)$$

As the y axis of the base of the orientation points in direction of increasing r , a coupling between Cartesian x / y velocities and rotational velocities of the manifold is given by

$$\mathbf{J}_{\omega\mathbf{x}} = \mathbf{R}^\top \begin{bmatrix} 0 & 0 & 0 \\ 0 & 0 & 0 \\ \frac{y}{x^2+y^2} & \frac{-x}{x^2+y^2} & 0 \end{bmatrix} \quad (78)$$

where \mathbf{R}^\top denotes the orientation in manifold coordinates.

2) *$\mathcal{S}^2 \times \mathbb{R}^1 \times \mathcal{S}^3$ Jacobian*: Cartesian x , y , z contribute to angular and r parts of \mathcal{M}_3

$$\mathbf{J}_{\mathbf{px}} = \begin{bmatrix} \frac{1}{r} & 0 & 0 \\ 0 & \frac{1}{r} & 0 \\ 0 & 0 & 1 \end{bmatrix} \cdot \mathbf{R}_{\text{align}}^\top \quad (79)$$

where $\mathbf{R}_{\text{align}}$ is the rotation matrix equivalent to $\mathbf{q}_{\text{align}}$. For the couplings, we get

$$\mathbf{J}_{\omega\mathbf{x}} = \mathbf{R}^\top \cdot \begin{bmatrix} 0 & \frac{1}{r} & 0 \\ -\frac{1}{r} & 0 & 0 \\ 0 & 0 & 0 \end{bmatrix} \cdot \mathbf{R}_{\text{align}}^\top \quad (80)$$

where \mathbf{R}^\top again denotes the orientation in manifold coordinates.